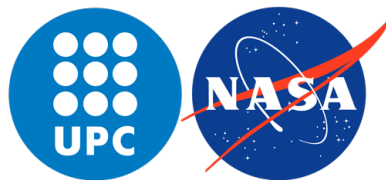

Analysis of the growth rate of heliospheric magnetic flux rope instabilities

NASA Goddard Space Flight Center
Heliophysics Science Division (HSD)

Universitat Politècnica de Catalunya
Degree in Mathematics - Degree in Engineering Physics



Samuel Capellas Coderque
Bachelor's Thesis

Supervisor (NASA GSFC): Teresa Nieves Chinchilla
Co-supervisor (UPC ETSETB): Juan Manuel Rius Casals

May 2022



UNIVERSITAT POLITÈCNICA DE CATALUNYA
BARCELONATECH

Facultat de Matemàtiques i Estadística



UNIVERSITAT POLITÈCNICA DE CATALUNYA
BARCELONATECH

Escola Tècnica Superior d'Enginyeria
de Telecomunicació de Barcelona



UNIVERSITAT POLITÈCNICA DE CATALUNYA
BARCELONATECH

Centre de Formació Interdisciplinària Superior



Abstract

English:

Heliospheric magnetic flux ropes (MFRs) have been found to be a fundamental internal structure of Interplanetary Coronal Mass Ejections (ICMEs). This work focuses on determining whether a given free-boundary flux rope structure is stable or not, by finding the rate at which an instability may evolve in time. The growth rate method was introduced by Linton et al. (1996) for the kink instability, and was applied by Florido-Llinas et al. (2020) to the forecasting of rotations in expanding ICMEs. In the present thesis, we work on the mathematical justification and the identification of the key assumptions behind this method, as well as generalizing it to analyze other plasma instabilities that affect the cross-section of the flux rope. Such a study has been applied to equilibrium magnetic field configurations inspired in the Gold-Hoyle model, in an attempt to explore whether the internal twist and Lorentz forces are related to the flux rope stability.

Català:

Les cordes de flux magnètic heliosfèriques (MFRs) són considerades les estructures internes fonamentals de les Ejeccions de Massa Coronal Interplanetàries (ICMEs). Aquest treball es centra en determinar si donada una corda de flux magnètic amb frontera lliure, aquesta és estable o no, trobant el ritme al qual una inestabilitat pot créixer en el temps. El mètode de la velocitat de creixement va ser introduït per Linton et al. (1996) per la inestabilitat de tipus kink, i va ser aplicat per Florido-Llinas et al. (2020) per la prediccio de rotacions en ICMEs en expansió. En la present tesi, treballem en la justificació matemàtica i la identificació de les assumpcions clau darrere aquest mètode, a la vegada que el generalitzem per tal d'analitzar altres inestabilitats del plasma que podem afectar a la secció transversal de la corda de flux magnètic. Aquest estudi ha estat aplicat a l'equilibri de configuracions de camp magnètic inspirades en el model de Gold-Hoyle, amb l'objectiu d'explorar si la torsió i forces de Lorentz estan relacionades amb l'estabilitat de les cordes de flux magnètic.

Castellano:

Las cuerdas de flujo magnético heliosféricas (MFRs) son consideradas las estructuras internas fundamentales de las Eyecciones de Masa Coronal Interplanetarias (ICMEs). Este trabajo se centra en determinar si dada una cuerda de flujo magnético con frontera libre, esta es estable o no, encontrando el ritmo al cual la inestabilidad puede crecer en el tiempo. El método de la velocidad de crecimiento fue introducido por Linton et al. (1996) para la inestabilidad de tipo kink, y fue aplicado por Florido-Llinas et al. (2020) para la predicción de rotaciones en ICMEs en expansión. En la presente tesis, trabajamos en la justificación matemática y la identificación de las asunciones clave detrás de este método, a la vez que lo generalizamos con el fin de analizar otras inestabilidades del plasma que pueden afectar a la sección transversal de la cuerda de flujo magnético. Este estudio ha sido aplicado al equilibrio de configuraciones de campo magnético inspiradas en el modelo de Gold-Hoyle, con el objetivo de explorar si la torsión y fuerzas de Lorentz están relacionadas con la estabilidad de las cuerdas de flujo magnético.

Keywords— magnetic flux ropes, coronal mass ejections, kink instability, growth rate

AMS2020 Code— 76E25, 85-10

Acknowledgements

I would like to start expressing my gratitude to Teresa Nieves Chinchilla, for welcoming me into NASA Goddard Space Flight Center and putting some much effort in guiding me through this exciting project. It really means a lot. I also want to extend my gratitude to the rest of the LASSOS team for teaching me, valuing me, and making me feel part of the team.

I also feel the need to thank CFIS and the Cellex Private Foundation for the financial support during this Mobility Program, and providing me with such an unbelievably great opportunity to grow and learn. In particular, thank you Toni Pascual Iserete for making this possible.

Moreover, I want to thank Marta Florido Llinàs for altruistically spending time chatting with me about her great work and answering every single one of my questions, helping me hit the ground running during this project.

Finally, I want to extend my gratitude to the rest of individuals who have worked by my side, helping me out whenever I needed a hand. Thank you Fernando Carcaboso Morales, Jordi Jumilla Lorenz, Andreas J. Weiss, Mark G. Linton, and my UPC mentor, Juan Manuel Rius Casals. And thank you to my family, who has sheared my dreams from day one. Your generosity is inspiring.

Contents

Introduction	1
1 Space plasmas and ideal MHD	2
1.1 Coronal Mass Ejections (CMEs)	2
1.2 The equations of Ideal Magnetohydrodynamics	5
1.3 Ideal gas law and plasma potential energy	6
2 General Plasma Stability	8
2.1 Introduction to linear stability	8
2.2 Linearized equation of motion	9
2.3 General solutions to the equation of motion	11
2.4 Inner product space of displacements	12
2.5 Self-adjointness of the force operator	13
2.6 Solutions to the Cauchy problem	14
2.7 Energy integral functionals	16
2.8 Growth rate of instabilities	18
2.9 Gateaux differentiation and quadratic forms	20
2.10 Determination of the growth rate	22
2.11 Potential energy for incompressible displacements	23
2.12 Differential inequality with exponential growth	24
3 Cylindrical Plasma Stability	26
3.1 Magnetic flux ropes as cylindrical plasmas	26
3.2 Fourier perturbation analysis	28
3.3 Expansion of the generalized energy	29
3.4 Optimization of the generalized energy	32
3.5 External perturbation solution	35
3.6 Free-boundary conditions: assumptions	36
3.7 Free-boundary conditions: equations	37
4 Application of the method	40
4.1 Magnetic flux rope modeling	40

4.2	The Gold-Hoyle modified model	41
4.3	Implementation of the growth rate method	43
4.4	Determining of the dispersion relation	44
4.5	Obtaining the maximum growth rate	45
4.6	Stability plots	47
5	Conclusions	49

Introduction

Coronal Mass Ejections (CMEs) are the structures dominating the transport of mass and energy from the Sun into the Heliosphere. Since their discovery in the 70s, understanding their formation and evolution has become one of the key priorities of space research. In the recent years, several studies are being conducted in order to understand their internal structure, and the instabilities they may develop.

The aim of the present work is to increase our theoretical understanding of the plasma instabilities that take place in Magnetic Flux Ropes (MFRs), the twisted flux tubes that constitute the internal magnetic structure of CMEs. We work on trying to give a formal background and generalizing an existing method for characterizing the stability of MFRs, which consists in finding the growth rate at which instabilities develop in time, by using cylindrical geometry and free-to-move boundary conditions for the equilibrium perturbation displacements. Such a method was presented in [Linton et al. \(1996\)](#) for the kink instability, and was then applied in [Florido-Llinas et al. \(2020\)](#) to study the potential causes of rotations in expanded CMEs.

In Chapter 1 we briefly present the context of this work, starting with CMEs themselves and presenting the Ideal Magnetohydrodynamics framework, which is used to describe space plasmas. Then, Chapter 2 is an attempt to provide a somewhat rigorous mathematical foundation to the growth rate method. In Chapter 3, we continue developing the method in a cylindrical geometry, determining the equations to analyze instabilities of any azimuthal wave number m . In Chapter 4, we provide an application of the method by using a newly developed MFR model.

1 . Space plasmas and ideal MHD

1.1 Coronal Mass Ejections (CMEs)

Coronal Mass Ejections (CMEs) are expulsions of magnetized plasma which are ejected from the Sun's corona into the Heliosphere. Their velocities can range from 250 Km/s up to 3000 Km/s, so that Earth directed CMEs can take from 15 hours to a few days to reach us. When a CME travels through the interplanetary medium, it is often denominated as a Interplanetary Coronal Mass Ejection (ICME).

The most fast and virulent CMEs usually take place during the maximum of the 11-year solar cycle, and originate in active regions of the Sun, or sunspot groups, where magnetic field lines and stressed magnetic flux accumulate enormous amounts of magnetic energy and then release it into the interplanetary medium through a process called *reconnection*. Nonetheless, the origin of CMEs is still a problem under study, and several other processes such as the MHD kink and torus instabilities also have been proposed as initiation mechanisms for CMEs.

Figure 1.1 shows an image of a CME eruption taken by NASA's Solar Dynamics Observatory, which also draws a comparison between the sizes of the ejected plasmas and the Earth. Terrifying. But when a CME reaches our planet, the Earth's magnetosphere shields off most of the incoming plasmas and radiation, often causing northern lights (aurora borealis) near the Earth's poles.

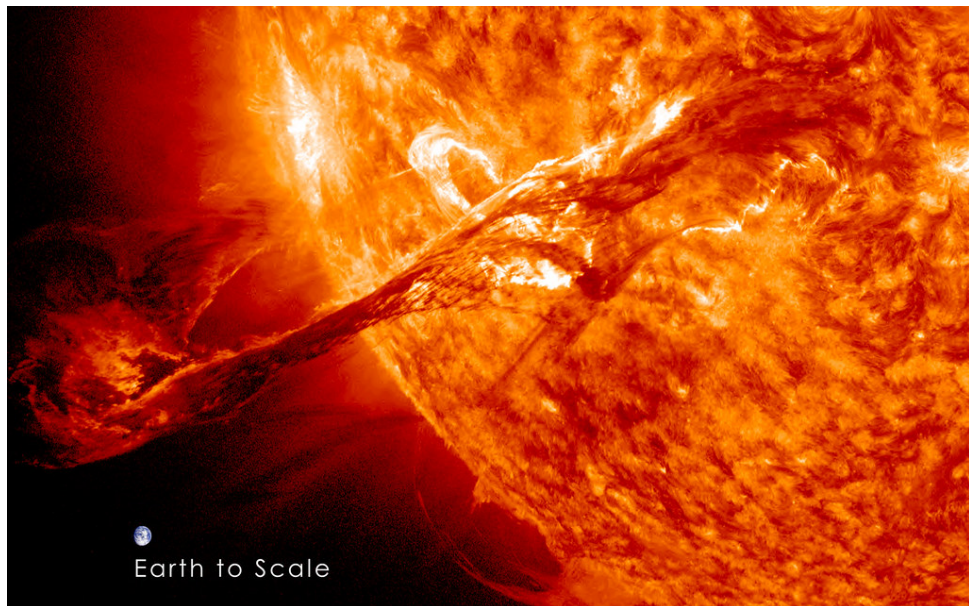


Figure 1.1: Eruption of a CME in August 31, 2012, at a speed of around 1500 Km/s. It was captured from NASA's Solar Dynamics Observatory (SDO). [Source](#).

Furthermore, our space technologies and astronauts find themselves in danger during the Earth arrival of an ICME. Hence, an accurate understanding of CME forecasting becomes a crucial

problem for humanity, and space agencies such as NASA are spending efforts and resources to learn more about these large scale structures.

Some of the most recent missions with a particular focus on CME study are Parker Solar Probe (NASA, launched 2018), Solar Orbiter (ESA-NASA, launched 2020). Their payloads are equipped to measure several plasma variables such as the magnetic fields, velocity, particle density, temperature and pressure¹. The data gathered is then processed to better understand their dynamics and internal configuration of CMEs. Figure 1.2 shows an example of processed data from [Masías-Meza et al. \(2016\)](#), where CMEs are classified in three classes depending on their speed, and their parameters are normalized and averaged to determine patterns in their structure.

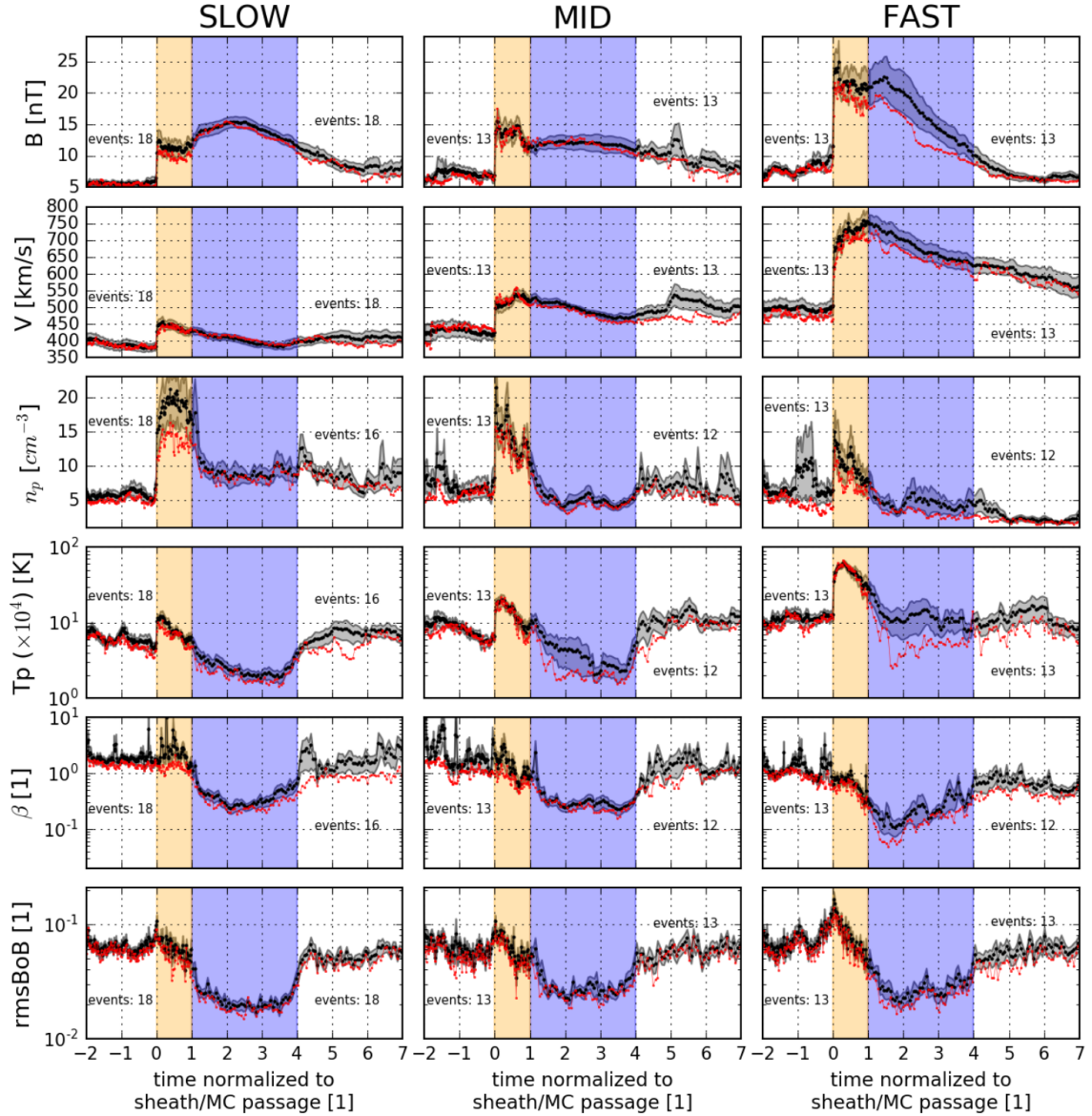


Figure 1.2: Classification of processed ICME data according to its velocity. From top to bottom, the plots show the magnetic field strength, velocity, proton density, proton temperature, plasma β and normalized magnetic-fluctuation density. The sheath of the ICME is colored in orange, and the MFR in purple. Black and red lines are used to represent average and median values, respectively. Extracted from [Masías-Meza et al. \(2016\)](#).

¹Measured through the plasma plasma β , which is the ratio of the plasma pressure to the magnetic pressure.

The previous plots differentiate between two key parts of an ICME: the *sheath*, which is a region of compressed plasma located at the front of the CME, and the *magnetic cloud*, which constitutes the rest of the structure.

Note than several key properties of CMEs are manifested in Figure 1.2:

- ◊ The magnetic field magnitude increases radically in the interior of the CME with respect to the ambient solar wind.
- ◊ ICMEs expand while traveling through the interplanetary medium: indeed, there is a discrepancy in the velocity at the front and the back part of the structure, the front velocity being greater.
- ◊ The plasma β is smaller inside a CME, so the magnetic forces rule the structure.

Other types of key experiments in CMEs include the use of magnetometers, which measure the three components of the magnetic field inside the structure. Such measured have revealed a characteristic structure inside magnetic clouds, which will be fundamental to this thesis: *Magnetic Flux Ropes* (MFRs). A MFR is defined as a twisted magnetic flux tube, that is, a twisted structure which has magnetic field lines wrapped around an axis.

Magnetic flux ropes, like many other plasma structures, may be prone to develop plasma instabilities which alter a previous state of equilibrium. One of these instabilities, called the *kink instability*, takes place when the MFR is curled around its axis, potentially inducing a radical change in the structure. In [Linton et al. \(1996\)](#), a method is developed to determine the rate at which such instabilities grow in time in an isolated flux ropes in the surface of the Sun, potentially causing the eruption of a CME. Such an event can be seen in Figure 1.3. Furthermore, [Florido-Llinas et al. \(2020\)](#) proposed the kink instability as a mechanism behind CME rotations with respect to the solar equator, that have been observed during their evolution (see [Vourlidas et al. \(2011\)](#)). However, in order to understand these (and also more general) plasma instabilities, one should start by introducing the main laws of physics ruling space plasmas: Ideal Magnetohydrodynamics.

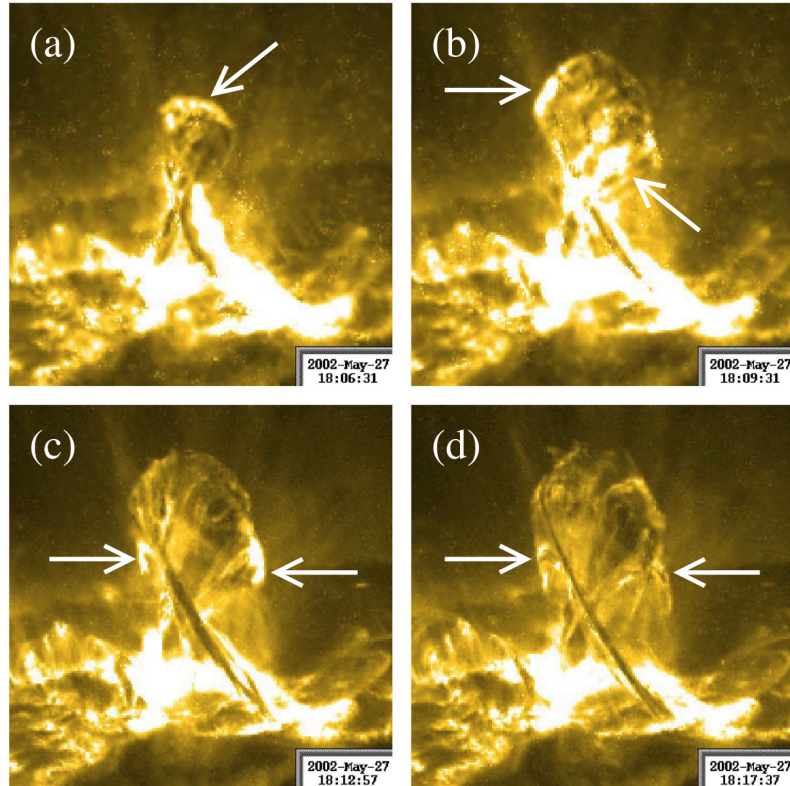


Figure 1.3: CME Eruption in May 2002, associated to the occurrence of the kink instability. Extracted from [Hassanin and Kliem \(2016\)](#).

1.2 The equations of Ideal Magnetohydrodynamics

A plasma is often described as an ionized gas, or a set of both charged and neutral particles with a correlated or collective behavior. However, in this work, the Ideal Magnetohydrodynamics (MHD) framework will be used, which simplifies the complex behavior of plasmas to the one of an electrically conducting fluid. Hence, Ideal MHD arises from the coupling of fluid mechanics and Maxwell equations. A very complete explanation on why plasmas show this behavior, and the details behind all the ideal MHD equations, can be found in [Priest \(2013\)](#) and [Florido-Llinas \(2020\)](#). In this work, we will briefly describe them, and take them as a starting to develop further theory in Chapter 2.

The first relevant equation is the Newton's *equation of motion* for a fluid element subject to a pressure gradient and electromagnetic forces. If it has pressure p , velocity \mathbf{v} , current density \mathbf{J} and magnetic field \mathbf{B} , the equation of motion reads

$$\rho \frac{D\mathbf{v}}{Dt} = \mathbf{J} \times \mathbf{B} - \nabla p, \quad (1.1)$$

where the material derivative

$$\frac{D}{Dt} = \frac{\partial}{\partial t} + \mathbf{v} \cdot \nabla \quad (1.2)$$

provides us with the temporal derivative of a magnitude as seen from the reference frame of the fluid, as can be intuitively seen through the chain rule. Note that gravitational forces are being ignored: this approximation is not always valid, it is for the studies of interest, involving the eruption and evolution of CMEs ([Hassanin and Kliem \(2016\)](#)).

The next ideal MHD equation is the induction equation, relating the partial derivative of the magnetic field \mathbf{B} with the field itself and the fluid velocity \mathbf{v} :

$$\frac{\partial \mathbf{B}}{\partial t} = \nabla \times (\mathbf{v} \times \mathbf{B}) \quad (1.3)$$

This equation is obtained from the combination of Faraday's and Ohm's law, and assuming the *ideal* limit of convective transport is satisfied, that is, the field lines are *frozen in*, or constrained to move with the plasma. This is commonly known as Alfvén's Theorem.

We also have *Ampere's law* for non-relativistic plasmas, relating the magnetic field \mathbf{B} and the current density \mathbf{J} :

$$\nabla \times \mathbf{B} = \mu_0 \mathbf{J}, \quad (1.4)$$

and the *Gauss' law for magnetism*, stating that \mathbf{B} must have zero divergence:

$$\nabla \cdot \mathbf{B} = 0. \quad (1.5)$$

On the hydrodynamics side of ideal MHD, another key equation is *entropy conservation*,

$$\frac{Dp}{Dt} + \gamma p \nabla \cdot \mathbf{v} = 0, \quad (1.6)$$

being p the fluid pressure and $\gamma = C_P/C_V$ the ratio of specific heats.

Finally, we have the *mass conservation* equation, also known as *continuity equation*, which states

$$\frac{D\rho}{Dt} + \rho \nabla \cdot \mathbf{v} = 0, \quad (1.7)$$

being ρ the mass density of the fluid. This expression for the continuity equation can be used to understand incompressible fluids, which turn out to be relevant to the study of ideal MHD plasma stability. Indeed, a fluid is said to be *incompressible* if the density of any *fluid parcel* (that is, any infinitesimal volume moving with the fluid) remains constant. Thus, equation (1.7) shows a fluid is incompressible if, and only if, $\nabla \cdot \mathbf{v} = 0$.

1.3 Ideal gas law and plasma potential energy

A plasma is made of both charged and neutral particles, which can have different individual particle densities n_i and temperature T_i . For instance, in heliospheric measurements, the proton density n_p and temperature T_p are measured, as we have seen in Figure 1.2. Then, a generalized *ideal gas law* is satisfied, where p is the total plasma pressure:

$$p = \sum_i n_i k_B T_i. \quad (1.8)$$

In this section, we will see two results which derive from this fact, and have useful applications to space plasmas.

Lemma 1.1. Let p be the plasma pressure, ρ its mass density, and m the mass of a proton. Then, we have:

$$p = \frac{\rho}{m} k_B T_0, \quad (1.9)$$

where T_0 is a *characteristic plasma temperature*, and depends on the spacial location. Furthermore, for the interior of a CME, it can be approximated through

$$T_0 \approx 1.7 \cdot 10^5 K. \quad (1.10)$$

Proof. The composition of the plasma in the solar wind is made of protons, electrons, and alpha particles (helium nuclei, with mass number equal to $4u$ and an electrostatic charge of $+2e$). As explained in Carcaboso et al. (2020), the alpha to proton ratio in the solar wind is

$$N_\alpha \approx 0.04 N_p. \quad (1.11)$$

Furthermore, for charge neutrality of the plasma (noticing the charge of α particles is $+2$):

$$N_e = 2N_\alpha + N_p \approx 1.08 N_p \quad (1.12)$$

Then, the density of the plasma, neglecting the mass of the electron ($m_e \approx 0$), can be related to the proton density through:

$$\rho = \frac{m_p N_p + m_e N_e + m_\alpha N_\alpha}{\text{volume}} \approx \frac{m_p N_p + 4m_p \cdot 0.04 N_p}{\text{volume}} = 1.16 \rho_p \quad (1.13)$$

This relation is especially useful when reading observational data, since it uses the proton density to obtain the fluid mass density, which is the one appearing in the ideal MHD equations, and is a crucial parameter to an ideal MHD plasma stability analysis.

On the other hand, using relations (1.11) and (1.12), and assuming the proton and alpha temperature are the same,

$$p = \sum_i n_i k_B T_i = n_p k_B (T_p + 1.08 T_e + 0.04 T_\alpha) \approx \frac{\rho}{1.16 m_p} k_B (1.04 T_p + 1.08 T_e), \quad (1.14)$$

which is the relation we wanted to show. As can be seen in Masías-Meza et al. (2016), the proton temperature T_p inside a CME depends on the point of space, but on average it is roughly given by $T_p \approx 4 \cdot 10^4 K$. The electron temperature can be taken as constant $T_e = 1.4 \cdot 10^5 K$, as mentioned in Section 3.2.1 of Carcaboso et al. (2020). This leads to

$$T_0 = \frac{1.04 T_p + 1.08 T_e}{1.16} \approx \frac{1.04 \cdot (4 \cdot 10^4 K) + 1.08 (1.4 \cdot 10^5 K)}{1.16} \approx 1.7 \cdot 10^5 K, \quad (1.15)$$

as we wanted to show. \square

Lemma 1.2. The potential energy of a plasma occupying a volume V is given by

$$W = \int_V \left(\frac{|\mathbf{B}|^2}{2\mu_0} + \frac{p}{\gamma - 1} \right) dV \quad (1.16)$$

The potential energy stored in a plasma is made up of magnetic energy, associated to its magnetic field, and internal energy, due to its gas nature. Firstly, the magnetic energy density, also known as magnetic pressure, is given by

$$p_B = \frac{|\mathbf{B}|^2}{2\mu_0}. \quad (1.17)$$

In order to find a suitable expression for the internal energy density, let m be the number of translational, rotational and vibrational degrees of freedom of the gas². The equipartition theorem states in the classical limit each degree of freedom of an ideal gas at temperature T contributes with an amount $k_B T/2$ to the internal energy of a gas, being k_B the Boltzmann constant. Assuming the plasma behaves as an ideal gas, its internal energy density is given by

$$u = m \sum_i n_i \frac{k_B T_i}{2} = \sum_i \frac{n_i k_B T_i}{\gamma - 1} \quad (1.18)$$

where n is the number of atoms per unit volume, and $\gamma = 1 + 2/m$ is known as the heat capacity ratio of the gas. Therefore, introducing the pressure P , we can use the ideal gas law (1.8) to obtain

$$u = \frac{p}{\gamma - 1}. \quad (1.19)$$

Finally, the potential energy of the plasma is obtained by integrating the energy density along the plasma volume. \square

²For instance, monoatomic gases possess $m = 3$ translational modes, and diatomic gases at room temperature have two additional rotational modes in the plane perpendicular to the molecule's axis, so $m = 5$.

2 . General Plasma Stability

2.1 Introduction to linear stability

This chapter is aimed at determining whether an ideal MHD plasma configuration with a general geometry, initially found in static equilibrium, is prone to develop an instability that may radically change its structure. Before going into details, we start by going through the concepts of equilibrium and linear stability, with a special focus on ideal MHD plasmas.

An *equilibrium state* of a system can be defined as a configuration where the present forces balance one another. Hence, as long as no external forces act on the system, its equilibrium state will remain unchanged, so that any quantity $\phi_0(\mathbf{r}, t)$ describing a system in equilibrium must have only spacial dependence, $\phi_0(\mathbf{r}, t) = \phi_0(\mathbf{r})$, or

$$\frac{\partial \phi_0}{\partial t} = 0. \quad (2.1)$$

An equilibrium state is said to be *static* if the system is found at rest. In the case of a fluid, this means the flow velocity in equilibrium is zero everywhere: $\mathbf{v}_0(\mathbf{r}) = 0$. An equilibrium can also be *dynamic* if there is motion, which should be at constant speed to ensure force balance is satisfied. While the assumption of a static equilibria is very plausible for laboratory fusion plasmas, its applicability to certain astrophysical plasmas can be questionable, as stated in [Goedbloed \(2018\)](#). Despite of this we will assume heliospheric magnetic flux ropes to be initially found in static equilibria in order to be consistent with some of the literature studying their instabilities ([Linton et al. \(1996\)](#), [Florido-Llinas et al. \(2020\)](#)), but such an assumption should be reviewed in the future.

An equilibrium state is said to be *stable* if any displacement induces a restoring force that makes the system evolve back to the same equilibrium. In contrast, if the force induced by a subset of displacements tends to amplify them and alter the morphology of the system, such an equilibrium is said to be *unstable*. Note that stability can also be characterized in energetic terms: stable equilibria are configurations which attain a minimal value of the potential energy of the system, while the potential energy of unstable equilibrium configurations can be decreased by displacing the system in a certain way.

Studying the stability of a system can be a tremendously difficult problem, depending on the complexity of the equations that characterize its dynamics. In the case of a plasma governed by ideal MHD, such equations have been explained in Chapter 1, and are summarized in Theorem 2.1 (page 9). Instead of attempting to find an exact solution to these equations, a common approach is to perform a *linear stability* analysis, where only infinitesimal displacements about an equilibrium configuration are considered, in contraposition to a *non-linear stability* analysis, where finite displacements are also contemplated. In other words, the aim of linear stability is determining whether an equilibrium state is a local minimum of the potential energy, while non-linear stability shall determine if it is a global minimum.

When studying linear stability, one must start by defining the time-independent variables $\{\phi_0(\mathbf{r})\}$ that define the equilibrium of the system and satisfy its equations. Then, each variable is perturbed about the equilibrium $\phi_0(\mathbf{r})$ through a *small* perturbation term $\phi_1(\mathbf{r}, t)$, that is, satisfying $\phi_1(\mathbf{r}, t) \ll \phi_0(\mathbf{r})$. Using this, and plugging the total variables $\phi(\mathbf{r}, t) = \phi_0(\mathbf{r}) + \phi_1(\mathbf{r}, t)$ in the system of equations, many simplifications can be made and the linear dynamics can be obtained.

2.2 Linearized equation of motion

In this section, the linear dynamics of an ideal MHD plasma are obtained. After being introduced in Bernstein et al. (1958), this derivation became standard in the literature; similar explanations can be found in Goedbloed and Poedts (2004) and Florido-Llinas (2020). We start by summarizing the equations governing an ideal MHD plasma system.

Theorem 2.1: Ideal MHD Equations. The dynamics of an ideal MHD plasma are given in terms of the flow velocity \mathbf{v} , magnetic field \mathbf{B} , pressure p and density ρ through the following nonlinear system of partial differential equations^a:

$$\rho \frac{D\mathbf{v}}{Dt} = \mathbf{J} \times \mathbf{B} - \nabla p, \quad \nabla \times \mathbf{B} = \mu_0 \mathbf{J}, \quad (\text{Eq of motion + Ampere's law}) \quad (2.2)$$

$$\frac{\partial \mathbf{B}}{\partial t} = \nabla \times (\mathbf{v} \times \mathbf{B}), \quad \nabla \cdot \mathbf{B} = 0, \quad (\text{Faraday's + Gauss' for EM laws}) \quad (2.3)$$

$$\frac{Dp}{Dt} + \gamma p \nabla \cdot \mathbf{v} = 0, \quad (\text{Entropy conservation}) \quad (2.4)$$

$$\frac{D\rho}{Dt} + \rho \nabla \cdot \mathbf{v} = 0. \quad (\text{Mass conservation}) \quad (2.5)$$

^aThe gravity term in the equation of motion has been neglected, as explained in Chapter 1

Proof. As explained in Chapter 1, the details and derivations of these equations can be found in the literature (Florido-Llinas (2020), Priest (2013)). These equations, when added to an appropriate set of boundary conditions, determines the evolution of the system. To see this, one can start by substituting Ampère's law into the equation of motion to eliminate \mathbf{J} , and continue by noticing that

$$\frac{\partial}{\partial t} (\nabla \cdot \mathbf{B}) = \nabla \cdot \left(\frac{\partial \mathbf{B}}{\partial t} \right) = \nabla \cdot (\nabla \times (\mathbf{v} \times \mathbf{B})) = 0, \quad (2.6)$$

so Gauss' law for electromagnetism only serves as an initial condition for the divergence of \mathbf{B} . Hence, one is left with a set of eight equations involving eight unidimensional unknown functions to be determined. \square

Theorem 2.2: Linearized equation of motion. Let $\boldsymbol{\xi}(\mathbf{r}, t)$ be the position displacement field of an ideal MHD plasma from a static equilibrium configuration, defined through the equilibrium quantities^a \mathbf{B} , ρ and p . Then, the equation of motion

$$\rho \frac{\partial^2 \boldsymbol{\xi}}{\partial t^2} = \mathbf{F}(\boldsymbol{\xi}) \quad (2.7)$$

holds, where the ideal MHD force $\mathbf{F}(\boldsymbol{\xi})$, representing the force done per unit volume while displacing the plasma, is determined by $\boldsymbol{\xi}$ and the equilibrium quantities through

$$\mathbf{F}(\boldsymbol{\xi}) = \frac{1}{\mu_0} (\nabla \times \mathbf{B}) \times \mathbf{Q}(\boldsymbol{\xi}) + \frac{1}{\mu_0} (\nabla \times \mathbf{Q}(\boldsymbol{\xi})) \times \mathbf{B} + \nabla (\boldsymbol{\xi} \cdot \nabla p + \gamma p \nabla \cdot \boldsymbol{\xi}). \quad (2.8)$$

We note by \mathbf{Q} the perturbation in the magnetic field, given by $\mathbf{Q}(\boldsymbol{\xi}) = \nabla \times (\boldsymbol{\xi} \times \mathbf{B})$.

^aThe subscript of the equilibrium quantities ϕ_0 is being dropped for simplicity.

Proof. Consider an ideal MHD plasma found in a static equilibrium state which is given by the time-independent fields $\mathbf{B}_0(\mathbf{r})$, $\rho_0(\mathbf{r})$ and $p_0(\mathbf{r})$. A static equilibrium implies $\mathbf{v}_0(\mathbf{r}) = 0$. Using Theorem 2.1, the equilibrium quantities must satisfy the relations:

$$\mathbf{J}_0 \times \mathbf{B}_0 = \nabla p_0, \quad \nabla \times \mathbf{B}_0 = \mu_0 \mathbf{J}_0, \quad \nabla \cdot \mathbf{B}_0 = 0. \quad (2.9)$$

The linear stability analysis continues by considering a *small* Eulerian perturbation¹ about the initial equilibrium, for each of the variables of the system:

$$\mathbf{B}(\mathbf{r}, t) = \mathbf{B}_0(\mathbf{r}) + \mathbf{B}_1(\mathbf{r}, t), \quad (2.10)$$

$$\mathbf{v}(\mathbf{r}, t) = \mathbf{v}_1(\mathbf{r}, t), \quad (2.11)$$

$$p(\mathbf{r}, t) = p_0(\mathbf{r}) + p_1(\mathbf{r}, t), \quad (2.12)$$

$$\rho(\mathbf{r}, t) = \rho_0(\mathbf{r}) + \rho_1(\mathbf{r}, t). \quad (2.13)$$

Note that the magnetic field perturbation leads to a perturbation in the current density, which is given in terms of the former through Ampere's law:

$$\mathbf{J}(\mathbf{r}, t) = \mathbf{J}_0(\mathbf{r}) + \mathbf{J}_1(\mathbf{r}, t), \quad \mathbf{J}_1 = \frac{1}{\mu_0} (\nabla \times \mathbf{B}_1). \quad (2.14)$$

Furthermore, Gauss' law tells us that $\nabla \cdot \mathbf{B}_1 = 0$. Now, we proceed to plug expressions (2.10) through (2.14) in the ideal MHD equations. These shall be simplified by using the equilibrium relations (2.9), as well as the fact that equilibrium variables ϕ_0 have no time dependence. We will also use the perturbations are *small*, so that only expressions up to first order in the perturbations are considered, that is,

$$\phi_1 \cdot \theta_1 \approx 0, \quad \boldsymbol{\varphi}_1 \cdot \nabla \theta_1 \approx 0, \quad \boldsymbol{\varphi}_1 \cdot \nabla \boldsymbol{\vartheta}_1 \approx 0, \quad (2.15)$$

for any variables $\phi, \theta, \boldsymbol{\varphi}, \boldsymbol{\vartheta}$. In particular, material derivatives of the perturbations are approximated by their partial derivatives. Hence, from the ideal MHD equations we get:

$$\rho_0 \frac{\partial \mathbf{v}_1}{\partial t} = \mathbf{J}_0 \times \mathbf{B}_1 + \mathbf{J}_1 \times \mathbf{B}_0 - \nabla p_1, \quad (2.16)$$

$$\frac{\partial \mathbf{B}_1}{\partial t} = \nabla \times (\mathbf{v}_1 \times \mathbf{B}_0), \quad (2.17)$$

$$\frac{\partial p_1}{\partial t} = -\mathbf{v}_1 \cdot \nabla p_0 - \gamma p_0 \nabla \cdot \mathbf{v}_1. \quad (2.18)$$

Note that mass conservation leads to a similar expression for ρ_1 , which only turns out to be useful if gravity is being considered in the equation of motion. The next step is to define the vector field measuring the position displacement of the plasma from its equilibrium position, which we note by $\boldsymbol{\xi}(\mathbf{r}, t)$, and is related to the velocity perturbation through

$$\mathbf{v}_1 = \frac{\partial \boldsymbol{\xi}}{\partial t}. \quad (2.19)$$

Furthermore, we set the origin in time at the point when the perturbation starts to grow but is still imperceptible, such that

$$\boldsymbol{\xi}(r, 0) = 0, \quad \frac{\partial \boldsymbol{\xi}}{\partial t}(r, 0) = \mathbf{v}_1(r, 0) \neq 0. \quad (2.20)$$

We can now plug (2.19) into equations (2.17) and (2.18), integrating them in time by recalling that, just like $\boldsymbol{\xi}$, the perturbations \mathbf{B}_1, ρ_1 and p_1 are initially zero since the perturbation is yet to develop. The following equations are obtained:

$$\mathbf{B}_1 = \nabla \times (\boldsymbol{\xi} \times \mathbf{B}_0), \quad (2.21)$$

$$p_1 = -\boldsymbol{\xi} \cdot \nabla p_0 - \gamma p_0 \nabla \cdot \boldsymbol{\xi}. \quad (2.22)$$

Thus, the perturbations have been expressed in terms of just equilibrium quantities and the position displacement $\boldsymbol{\xi}$. These expressions can now be plugged into (2.16), together with (2.14) and (2.19), to obtain the desired linearized equation of motion (2.7) after dropping the subscripts and writing \mathbf{Q} instead of \mathbf{B}_1 . \square

¹In contraposition with a Lagrangian perturbation, which would use the reference system of the fluid in motion.

2.3 General solutions to the equation of motion

Once the linearized equation of motion has been derived, it is time to study which displacement $\xi(\mathbf{r}, t)$ are a solution it, given the appropriate initial conditions. The equation writes

$$\rho \frac{\partial^2 \xi}{\partial t^2} = \mathbf{F}(\xi), \quad (2.23)$$

where \mathbf{F} is the ideal MHD force operator defined in (2.8), taking the equilibrium magnetic field \mathbf{B} and the equilibrium pressure p as parameters. However, rather than \mathbf{F} , the operator $\rho^{-1}\mathbf{F}$ is usually more relevant from a theoretical point of view, and the following theorem sheds some light on why this is the case. It is also key to observe that these operators are linear in ξ , and that they can be applied to any function of space, not necessarily time-dependent. Let's start with a short definition.

Definition. A function $\xi : \mathbb{R}^3 \times [0, +\infty) \rightarrow \mathbb{C}^3$ is said to be *separable* if there is a pair of complex-valued functions $\mathbf{R} : \mathbb{R}^3 \rightarrow \mathbb{C}^3$ and $T : [0, +\infty) \rightarrow \mathbb{C}^3$ such that $\xi(\mathbf{r}, t) = \mathbf{R}(\mathbf{r})T(t)$.

Theorem 2.3. A separable displacement $\xi(\mathbf{r}, t)$ is a solution to the equation of motion (2.7) if, and only if, it can be expressed as

$$\xi(\mathbf{r}, t) = \xi_n(\mathbf{r}) (\alpha e^{i\omega_n t} + \beta e^{-i\omega_n t}), \quad (2.24)$$

where $\xi_n : \mathbb{R}^3 \rightarrow \mathbb{C}^3$ is an eigenfunction of the operator $\rho^{-1}\mathbf{F}$, and $-\omega_n^2$ is its eigenvalue:

$$\rho^{-1}\mathbf{F}(\xi_n) = -\omega_n^2 \xi_n. \quad (2.25)$$

The constants $\alpha, \beta \in \mathbb{C}$ depend on the initial conditions.

Proof. We plug a general separable displacement $\xi(\mathbf{r}, t) = \mathbf{R}(\mathbf{r})T(t)$ in the equation of motion:

$$\mathbf{R}(\mathbf{r}) \ddot{T}(t) = \rho^{-1}\mathbf{F}(\mathbf{R}(\mathbf{r})) T(t), \quad (2.26)$$

Such an equality must hold for any values \mathbf{r} and t , so there must exist a constant, which we write as $-\omega_n^2$ for some $\omega_n \in \mathbb{C}$, such that

$$\rho^{-1}\mathbf{F}(\mathbf{R}(\mathbf{r})) = -\omega_n^2 \mathbf{R}(\mathbf{r}) \quad (2.27)$$

$$\ddot{T}(t) = -\omega_n^2 T(t). \quad (2.28)$$

We find $\mathbf{R}(\mathbf{r})$ is an eigenfunction of $\rho^{-1}\mathbf{F}$ with eigenvalue $-\omega_n^2$, so we can note $\mathbf{R}(\mathbf{r}) = \xi_n(\mathbf{r})$. Furthermore, solving the differential equation for T , we obtain that

$$\xi(\mathbf{r}, t) = \xi_n(\mathbf{r}) (\alpha e^{i\omega_n t} + \beta e^{-i\omega_n t}). \quad (2.29)$$

Conversely, it is easy to check that any displacement of the form (2.24) is a solution to the equation of motion:

$$\frac{\partial^2 \xi}{\partial t^2}(\mathbf{r}, t) = -\omega_n^2 \xi_n(\mathbf{r}) (\alpha e^{i\omega_n t} + \beta e^{-i\omega_n t}) = \rho^{-1}\mathbf{F}(\xi(\mathbf{r}, t)) \quad (2.30)$$

where the linearity of $\rho^{-1}\mathbf{F}$ has been employed. \square

Comment. The linearity of $\rho^{-1}\mathbf{F}$ also implies that any linear combination of functions of the form (2.24),

$$\xi(\mathbf{r}, t) = \sum_n \xi_n(\mathbf{r}) e^{i\omega_n t}, \quad (2.31)$$

is a general solution to the equation of motion. Note that the summation has been re-indexed, so that both positive and negative exponential terms are being included as different terms in the summation. Such terms, as well as the eigenfunctions ξ_n , are often referred to as *normal modes* since they will be shown to be orthogonal to each other with respect to a certain inner product.

2.4 Inner product space of displacements

Once the issue of temporal variation has been tackled, one needs to describe accurately what set of functions $\xi(\mathbf{r})$ the operator $\rho^{-1}\mathbf{F}$ is acting on. We will define the set of all possible displacements to be the set of smooth functions with compact support², $\mathcal{C}_c^\infty(\mathbb{R}^3)$, which is an inner product subspace of the Hilbert space $\mathbf{L}_\rho^2(\mathbb{R}^3)$. Having defined an inner product between displacements will soon prove to be of great use to develop solid theoretical grounds of this stability analysis.

Definition. An *inner product space* is a real or complex vector space equipped with an inner product. A *Hilbert space* is an inner product space the metric space induced by which is complete, that is, every Cauchy sequence of points in the space converges to an element of the space.

Definition. In the context of ideal MHD linear stability, the literature³ considers plasma displacements belonging to the Hilbert space of *square integrable vector functions* over \mathbb{R}^3 , weighted by a scalar positive function $\rho : \mathbb{R}^3 \rightarrow [a, +\infty) \subset \mathbb{R}$, with $a > 0$. This space is noted as $\mathbf{L}_\rho^2(\mathbb{R}^3)$, and it is constituted by the complex vector functions $\xi : \mathbb{R}^3 \rightarrow \mathbb{C}^3$ that are square integrable with respect to ρ , that is, satisfying

$$\int \rho |\xi|^2 dV < \infty, \quad (2.32)$$

where the volume integral is performed over \mathbb{R}^3 . These functions are equipped with the weighted inner product

$$\langle \xi, \eta \rangle = \frac{1}{2} \int \rho \xi^* \cdot \eta dV \quad \text{for } \xi, \eta \in \mathbf{L}_\rho^2(\mathbb{R}^3), \quad (2.33)$$

which is guaranteed to be finite due to the Cauchy-Schwartz inequality,

$$\langle \xi, \eta \rangle^2 \leq \|\xi\|^2 \|\eta\|^2 < \infty. \quad (2.34)$$

The (finite) norm of any element $\xi \in \mathbf{L}_\rho^2(\mathbb{R}^3)$ has been defined as $\|\xi\|^2 = \langle \xi, \xi \rangle$.

Comment. If one provides ρ with some conditions which are not too restrictive, such as continuity and compact support, the set of functions $\mathbf{L}_\rho^2(\mathbb{R}^3)$ can be checked to be independent of the choice of weight function. For this work, we will use the plasma equilibrium density ρ as a weight.

Comment. One may realize that some functions $\xi \in \mathbf{L}_\rho^2(\mathbb{R}^3)$ are not suitable for the study of plasma stability. Indeed, expression (2.8) for \mathbf{F} requires all displacements ξ to be at least twice differentiable in order to evaluate the force done while displacing the plasma, $\mathbf{F}(\xi)$. Furthermore, some functions of this Hilbert space may take non-zero values at arbitrarily large distances of the origin, which contradicts the intuition of what an equilibrium displacement for usually bounded plasma structure should be. We thus need to restrict this space to a subspace of displacements that are physically feasible.

Definition. The space of *physical* displacements defined in this work is $\mathcal{C}_c^\infty(\mathbb{R}^3)$, the *smooth complex vector functions with compact support*, often known as *test functions*. We are thus providing the smoothness required by the operator $\rho^{-1}\mathbf{F}$, as well as guaranteeing the perturbations are localized, vanishing at locations that are far away from the plasma structure.

Comment. It is easy to prove that $\mathcal{C}_c^\infty(\mathbb{R}^3) \subset \mathbf{L}_\rho^2(\mathbb{R}^3)$ is a complex vector space of functions, which becomes an inner product space with the product inherited from $\mathbf{L}_\rho^2(\mathbb{R}^3)$. Although this new space is not a Hilbert space due to the lack of completeness, it is dense⁴ in its embedding Hilbert space. In fact, if $\Omega \subset \mathbb{R}^n$ an open subset, the space of test functions $\mathcal{C}_c^\infty(\Omega)$ is dense in $\mathbf{L}^p(\Omega)$ for $1 \leq p < \infty$ (Hunter (2014)). This property, setting $\Omega = \mathbb{R}^3$ and $p = 2$, will turn out to be particularly useful in the following section.

Comment. The elements of $\mathcal{C}_c^\infty(\mathbb{R}^3)$ are space functions but, as we have previously seen, we are interested in time-varying plasma displacements $\xi(\mathbf{r}, t)$. These can be seen as trajectories within $\mathcal{C}_c^\infty(\mathbb{R}^3)$ which, for every time t_0 , yield a certain test function $\xi(\mathbf{r}, t_0) \in \mathcal{C}_c^\infty(\mathbb{R}^3)$.

²A function is said to have *compact support* if it vanishes outside of a compact set.

³For example, Goedbloed and Poedts (2004) and Lifschitz (1989).

⁴ A is a *dense* subset of a topological space X if the smallest closed subset of X which contains A is X .

2.5 Self-adjointness of the force operator

The next step after introducing the inner product space of physical displacements is to introduce the self-adjointness of the force operator, which constitutes one of the main pillars of ideal MHD linear stability. Later in the section, we continue to present some of its most direct consequences.

Definition. Let \mathbf{S} be a complex inner product space. A linear operator $\mathbf{L} : \mathbf{S} \rightarrow \mathbf{S}$ is said to be *self-adjoint* if it is equal to its own adjoint:

$$\langle \boldsymbol{\xi}, \mathbf{L}(\boldsymbol{\eta}) \rangle = \langle \mathbf{L}(\boldsymbol{\xi}), \boldsymbol{\eta} \rangle \quad (2.35)$$

for any $\boldsymbol{\xi}, \boldsymbol{\eta} \in \mathbf{S}$.

Theorem 2.4. The operator $\rho^{-1}\mathbf{F} : \mathcal{C}_c^\infty(\mathbb{R}^3) \rightarrow \mathcal{C}_c^\infty(\mathbb{R}^3)$ is self-adjoint.

Proof. Firstly, assuming the equilibrium variables \mathbf{B} and p are smooth over \mathbb{R}^3 , we obtain

$$\rho^{-1}\mathbf{F}(\boldsymbol{\xi}) \in \mathcal{C}^\infty(\mathbb{R}^3) \text{ for any } \boldsymbol{\xi} \in \mathcal{C}_c^\infty(\mathbb{R}^3). \quad (2.36)$$

Furthermore, it is clear that wherever $\boldsymbol{\xi}$ vanishes, so does $\rho^{-1}\mathbf{F}(\boldsymbol{\xi})$, so $\rho^{-1}\mathbf{F}$ preserves compact support, and it is well defined in $\mathcal{C}_c^\infty(\mathbb{R}^3)$.

Secondly, the operator is linear. Indeed, for any $\alpha, \beta \in \mathbb{C}$ and $\boldsymbol{\xi}, \boldsymbol{\eta} \in \mathcal{C}_c^\infty(\mathbb{R}^3)$ the relation

$$\rho^{-1}\mathbf{F}(\alpha\boldsymbol{\xi} + \beta\boldsymbol{\eta}) = \alpha\rho^{-1}\mathbf{F}(\boldsymbol{\xi}) + \beta\rho^{-1}\mathbf{F}(\boldsymbol{\eta}) \quad (2.37)$$

holds due to the linearity of the divergence, gradient and curl operators. Finally, one is left to prove that for any $\boldsymbol{\xi}, \boldsymbol{\eta} \in \mathcal{C}_c^\infty(\mathbb{R}^3)$, the equality $\langle \boldsymbol{\xi}, \rho^{-1}\mathbf{F}(\boldsymbol{\eta}) \rangle = \langle \rho^{-1}\mathbf{F}(\boldsymbol{\xi}), \boldsymbol{\eta} \rangle$ is satisfied, namely:

$$\frac{1}{2} \int \boldsymbol{\xi}^* \cdot \mathbf{F}(\boldsymbol{\eta}) \, dV = \frac{1}{2} \int \boldsymbol{\eta} \cdot \mathbf{F}(\boldsymbol{\xi}^*) \, dV. \quad (2.38)$$

The proof of this property consists of expressing the product $\boldsymbol{\xi}^* \cdot \mathbf{F}(\boldsymbol{\eta})$ as a symmetric expression in $\boldsymbol{\xi}^*$ and $\boldsymbol{\eta}$, which requires tedious and cumbersome algebraic manipulations that have been carefully explained in sections 6.2.3 and 6.6.2 of [Goedbloed and Poedts \(2004\)](#). \square

Lemma 2.5. Let \mathbf{S} be a complex inner product space and \mathbf{L} a linear operator in \mathbf{S} . If \mathbf{L} is self-adjoint, its eigenvalues are real and its eigenfunctions having different eigenvalues are orthogonal to each other.

Proof. This proof is well known and can be found in any basic algebra text book. Let $\boldsymbol{\xi}$ be an eigenfunction of \mathbf{L} , with λ as its eigenvalue. Then:

$$0 = \langle \mathbf{L}(\boldsymbol{\xi}), \boldsymbol{\xi} \rangle - \langle \boldsymbol{\xi}, \mathbf{L}(\boldsymbol{\xi}) \rangle = \langle \lambda\boldsymbol{\xi}, \boldsymbol{\xi} \rangle - \langle \boldsymbol{\xi}, \lambda\boldsymbol{\xi} \rangle = (\lambda^* - \lambda) \|\boldsymbol{\xi}\|^2, \quad (2.39)$$

which proves $\lambda \in \mathbb{R}$. Now, let $\boldsymbol{\eta}$ be another eigenfunction of \mathbf{L} , with eigenvalue $\mu \neq \lambda$. Using the self-adjointness property once more:

$$0 = \langle \mathbf{L}(\boldsymbol{\xi}), \boldsymbol{\eta} \rangle - \langle \boldsymbol{\xi}, \mathbf{L}(\boldsymbol{\eta}) \rangle = \langle \lambda\boldsymbol{\xi}, \boldsymbol{\eta} \rangle - \langle \boldsymbol{\xi}, \mu\boldsymbol{\eta} \rangle = (\lambda - \mu) \langle \boldsymbol{\xi}, \boldsymbol{\eta} \rangle, \quad (2.40)$$

which implies the orthogonality condition $\langle \boldsymbol{\xi}, \boldsymbol{\eta} \rangle = 0$. \square

Corollary 2.6. The eigenvalues $-\omega_n^2$ of $\rho^{-1}\mathbf{F}$ are real. Hence, ω_n must be either real or purely imaginary. Furthermore, its eigenfunctions $\boldsymbol{\xi}_n$ having different eigenvalues are orthogonal to each other (hence, they are called *normal modes*).

Definition. A normal mode ξ_n is said to be *stable* or *unstable* depending on the sign of its corresponding (real) eigenvalue⁵.

- ◊ Stable normal modes: $\omega^2 \geq 0$. Indeed, if $\omega_n^2 > 0$, then $\omega \in \mathbb{R}$, and the time evolution of the normal mode will be oscillatory around its amplitude ξ_n . If $\omega_n^2 = 0$, the normal mode will remain constant. In both cases, the normal mode remains small when compared to the scale of the system.
- ◊ Unstable normal modes: $\omega_n^2 < 0$. In such case ω_n is imaginary, and the normal mode will grow exponentially, potentially inducing a larger scale instability.

Before ending this section, we present a result which is tightly related to the self-adjointness of $\rho^{-1}\mathbf{F}$, and is key to study the Cauchy problem associated to the equation of motion.

Lemma 2.7. If the spectrum of $\rho^{-1}\mathbf{F} : \mathcal{C}_c^\infty(\mathbb{R}^3) \rightarrow \mathcal{C}_c^\infty(\mathbb{R}^3)$ is discrete, any function $\xi \in \mathcal{C}_c^\infty(\mathbb{R}^3)$ can be expressed as an infinite linear combination of its eigenfunctions $\{\xi_n\}$.

Proof. This is a consequence of an analysis result:

Let \mathbf{L} be a self-adjoint operator defined on a dense domain \mathcal{D} in a Hilbert space \mathbf{H} . If \mathbf{L} has a discrete spectrum, then there exists an orthonormal set of eigenfunctions of \mathbf{L} that span all of \mathbf{H} . – [Karniadakis \(2015\)](#).

In order to use this result, we take $\mathbf{L} = \rho^{-1}\mathbf{F}$, $\mathcal{D} = \mathcal{C}_c^\infty(\mathbb{R}^3)$ and $\mathbf{H} = \mathbf{L}^2(\mathbb{R}^3)$. Indeed, we have seen in Theorem 2.4 that $\rho^{-1}\mathbf{F}$ is self-adjoint in $\mathcal{C}_c^\infty(\mathbb{R}^3)$. Furthermore, as mentioned in Section 2.4, $\mathcal{C}_c^\infty(\mathbb{R}^3)$ is dense subspace of $\mathbf{L}^2(\mathbb{R}^3)$ ([Hunter \(2014\)](#)). Therefore, we conclude the eigenfunctions $\{\xi_n\}$ span the whole space Hilbert space $\mathbf{L}^2(\mathbb{R}^3)$. In particular, the desired result is obtained. \square

Comment. The result we have used can be seen as one of the infinite dimensional generalizations of the spectral theorem for hermitian matrices. There are other versions which, instead of the discrete spectrum, require the operator to be compact, see [Smith \(2015\)](#). Nonetheless, $\rho^{-1}\mathbf{F}$ is not likely to be compact, since operators involving differentiation are usually unbounded.

Comment. During the rest of the chapter, we will assume a discrete spectrum for $\rho^{-1}\mathbf{F}$. However, the discrete spectrum hypothesis can also be problematic since, as explained in [Goedbloed and Poedts \(2004\)](#), the ideal MHD spectrum can be continuous. One may try to determine whether this is the case depending on the equilibrium functions \mathbf{B} and p , but such a discussion lies beyond the scope of this work.

2.6 Solutions to the Cauchy problem

Definition. Let $\mathbf{f}, \mathbf{g} \in \mathcal{C}_c^\infty(\mathbb{R}^3)$ be a pair of initial conditions. A *perturbation trajectory* is a solution $\xi(\mathbf{r}, t)$ to the following Cauchy problem:

$$\rho \frac{\partial^2 \xi}{\partial t^2} = \mathbf{F}(\xi), \quad \begin{cases} \xi(\mathbf{r}, 0) = \mathbf{f}(\mathbf{r}), \\ \frac{\partial \xi}{\partial t}(\mathbf{r}, 0) = \mathbf{g}(\mathbf{r}). \end{cases} \quad (2.41)$$

Comment. The existence of a solution to this problem will be proven, but the uniqueness will be taken as an assumption. Indeed, it is reasonable to expect the initial conditions to uniquely determine the dynamics of the system. Moreover, this step will be key to justify the following result, which was originally presented as the *completeness* hypothesis in [Bernstein et al. \(1958\)](#).

⁵The fact that $-\omega_n^2 \in \mathbb{R}$ implies that normal modes cannot be damped or exhibit overstability.

Theorem 2.8. Every perturbation trajectory can be expressed as a superposition of normal modes:

$$\boldsymbol{\xi}(\mathbf{r}, t) = \sum_n \boldsymbol{\xi}_n(\mathbf{r}) (\alpha_n e^{i\omega_n t} + \beta_n e^{-i\omega_n t}). \quad (2.42)$$

Proof. Since we have already seen in Section 2.3 that (2.42) is a general solution to the equation of motion, we only need to verify the existence of a set of values for α_n and β_n that ensure $\boldsymbol{\xi}(\mathbf{r}, t)$ also satisfies the initial conditions. Then, using the uniqueness of solutions for the Cauchy problem (2.41), we will conclude that any perturbation trajectory can be expressed in this form.

Hence, let $\mathbf{f}, \mathbf{g} \in \mathcal{C}_c^\infty(\mathbb{R}^3)$ be the boundary conditions for the trajectory under consideration. Lemma 2.7 can be used to express \mathbf{f} and \mathbf{g} in terms of the eigenfunctions $\boldsymbol{\xi}_n$,

$$\mathbf{f}(\mathbf{r}) = \sum_n \gamma_n \boldsymbol{\xi}_n(\mathbf{r}), \quad \mathbf{g}(\mathbf{r}) = \sum_n \delta_n \boldsymbol{\xi}_n(\mathbf{r}), \quad (2.43)$$

where $\gamma_n, \delta_n \in \mathbb{C}$ are given complex coefficients. Imposing the initial conditions, we get a linear system of equations which can be solved for α_n, β_n , assuming $\omega_n \neq 0$:

$$\begin{cases} \alpha_n + \beta_n = \gamma_n \\ i\omega_n (\alpha_n - \beta_n) = \delta_n \end{cases} \implies \alpha_n = \frac{1}{2} \left(\gamma_n - i \frac{\delta_n}{\omega_n} \right), \quad \beta_n = \frac{1}{2} \left(\gamma_n + i \frac{\delta_n}{\omega_n} \right). \quad (2.44)$$

This concludes the proof. \square

Comment. We can now find an expression for $\boldsymbol{\xi}(\mathbf{r}, t)$ in terms of the initial conditions, by plugging the expressions for α_n and β_n into (2.42), and using the following relations for $x \in \mathbb{C}$:

$$\cos(x) = \frac{e^{ix} + e^{-ix}}{2} = \cosh(ix), \quad \sin(x) = \frac{e^{ix} - e^{-ix}}{2i} = -i \sinh(ix). \quad (2.45)$$

This leads to

$$\boldsymbol{\xi}(\mathbf{r}, t) = \sum_n \boldsymbol{\xi}_n(\mathbf{r}) \left(\gamma_n \cos(\omega_n t) + \frac{\delta_n}{\omega_n} \sin(\omega_n t) \right). \quad (2.46)$$

Note that for the case of an initial static equilibrium, which has been considered since the start of this chapter, corresponds to $\gamma_n = 0$ for all n . Furthermore, recalling ω_n is either real or imaginary, and letting $\sigma_n = |\omega_n|$ in the latter case, we get:

$$\boldsymbol{\xi}(\mathbf{r}, t) = \sum_{\omega_n^2 > 0} \boldsymbol{\xi}_n(\mathbf{r}) \frac{\delta_n}{\omega_n} \sin(\omega_n t) + \sum_{\omega_n^2 < 0} \boldsymbol{\xi}_n(\mathbf{r}) \frac{\delta_n}{\omega_n} \sinh(\sigma_n t). \quad (2.47)$$

Finally, if the constant δ_n/ω_n is included as part of the eigenfunctions, a neater expression is obtained in terms of a stabilizing term and a destabilizing one.

$$\boldsymbol{\xi}(\mathbf{r}, t) = \sum_{\omega_n^2 > 0} \boldsymbol{\xi}_n(\mathbf{r}) \sin(\omega_n t) + \sum_{\omega_n^2 < 0} \boldsymbol{\xi}_n(\mathbf{r}) \sinh(\sigma_n t). \quad (2.48)$$

Comment. The partial differential equation above may also require a boundary condition for the solution to be fully determined. In our case, following Linton et al. (1996), we are interested in localized free-boundary solutions, so we impose the solution should vanish at infinity. This is automatically fulfilled by the functions $\boldsymbol{\xi}_n$ because of their compact support. Although an infinite linear combination of compactly supported functions does not necessarily vanish at infinity, we will assume this one does, so that $\boldsymbol{\xi}(\mathbf{r}, t) \in \mathcal{C}_c^\infty(\mathbb{R}^3)$ for any time $t \geq 0$.

Definition. A plasma equilibrium configuration is said to be *unstable* if there exists a perturbation trajectory $\boldsymbol{\xi}(\mathbf{r}, t)$ such that $\|\boldsymbol{\xi}(\mathbf{r}, t)\| \rightarrow +\infty$ as $t \rightarrow +\infty$ (for any \mathbf{r}), and *stable* otherwise.

Comment. The plasma is unstable if there is an unstable normal mode, and stable otherwise. Indeed, if there is an unstable normal mode, there will clearly exist a trajectory with a norm tending to infinity. Conversely, if all normal modes are stable, in Lemma 2.9 we show the norm of the trajectory must also be bounded (under a certain convergence condition).

Lemma 2.9. Consider a plasma in equilibrium where all normal modes are stable, $\omega_n \in \mathbb{R}$. Consider also an arbitrary perturbation trajectory^a, which using the completeness result in Theorem 2.8, it can be expressed as

$$\boldsymbol{\xi}(t) = \sum_n \boldsymbol{\xi}_n (\alpha_n e^{i\omega_n t} + \beta_n e^{-i\omega_n t}). \quad (2.49)$$

The normal modes $\{\boldsymbol{\xi}_n\}$ can be taken to be orthonormal. Then, assuming the convergence of the series

$$\|\boldsymbol{\alpha}\|^2 = \sum_n |\alpha_n|^2, \quad \|\boldsymbol{\beta}\|^2 = \sum_n |\beta_n|^2, \quad (2.50)$$

the trajectory's norm can be bounded as $\|\boldsymbol{\xi}(t)\| \leq \|\boldsymbol{\alpha}\| + \|\boldsymbol{\beta}\|$ for all $t \geq 0$.

^aThe spacial dependence is omitted to ease the notation.

Proof. Developing the norm through the scalar product and using $\langle \boldsymbol{\xi}_n, \boldsymbol{\xi}_m \rangle = \delta_{nm}$:

$$\|\boldsymbol{\xi}(t)\|^2 = \sum_n |\alpha_n e^{i\omega_n t} + \beta_n e^{-i\omega_n t}|^2 = \sum_n (|\alpha_n|^2 + |\beta_n|^2 + \alpha_n \beta_n^* e^{2i\omega_n t} + \alpha_n^* \beta_n e^{-2i\omega_n t}). \quad (2.51)$$

Using the inequality $x \leq |x|$ for $x \in \mathbb{R}$, and recalling that $|y+z| \leq |y| + |z|$ for $y, z \in \mathbb{C}$:

$$\alpha_n \beta_n^* e^{2i\omega_n t} + \alpha_n^* \beta_n e^{-2i\omega_n t} \leq |\alpha_n \beta_n^* e^{2i\omega_n t}| + |\alpha_n^* \beta_n e^{-2i\omega_n t}| = 2|\alpha_n||\beta_n|, \quad (2.52)$$

which leads to

$$\|\boldsymbol{\xi}(t)\|^2 \leq \sum_n (|\alpha_n|^2 + |\beta_n|^2 + 2|\alpha_n||\beta_n|) = \|\boldsymbol{\alpha}\|^2 + \|\boldsymbol{\beta}\|^2 + 2 \sum_n |\alpha_n||\beta_n|. \quad (2.53)$$

Note the Cauchy-Schwartz inequality for series yields

$$\sum_n |\alpha_n||\beta_n| \leq \left(\sum_n |\alpha_n|^2 \right)^{1/2} \left(\sum_n |\beta_n|^2 \right)^{1/2} = \|\boldsymbol{\alpha}\| \|\boldsymbol{\beta}\|, \quad (2.54)$$

and substituting this into (2.53),

$$\|\boldsymbol{\xi}(t)\|^2 \leq \|\boldsymbol{\alpha}\|^2 + \|\boldsymbol{\beta}\|^2 + 2\|\boldsymbol{\alpha}\| \|\boldsymbol{\beta}\| = (\|\boldsymbol{\alpha}\| + \|\boldsymbol{\beta}\|)^2 \quad (2.55)$$

as desired. \square

2.7 Energy integral functionals

In this section, we introduce algebraic expressions for the kinetic energy and the change in potential energy of the plasma, when undergoing a displacement $\boldsymbol{\xi}(\mathbf{r}, t)$ from equilibrium. These functionals have rich properties which turn out to be very helpful when studying ideal MHD linear stability. We will also see how the conservation of energy in linear ideal MHD follows from the self-adjointness of $\rho^{-1} \mathbf{F}$, making this property even more crucial.

Definition. The *kinetic energy* functional is given by

$$K(\boldsymbol{\xi}) = \frac{1}{2} \int \rho |\dot{\boldsymbol{\xi}}|^2 dV = \langle \dot{\boldsymbol{\xi}}, \dot{\boldsymbol{\xi}} \rangle, \quad (2.56)$$

where $\dot{\boldsymbol{\xi}}$ is short for the partial time derivative of $\boldsymbol{\xi}(\mathbf{r}, t)$, that is, the perturbation velocity. Note that the equilibrium has been defined to be static, so this expression represents all the kinetic energy of the plasma.

Definition. The *potential energy* functional is given by

$$W(\xi) = -\frac{1}{2} \int \xi^* \cdot \mathbf{F}(\xi) dV = -\langle \xi, \rho^{-1} \mathbf{F}(\xi) \rangle. \quad (2.57)$$

This quantity represents the change in potential energy with respect to the equilibrium configuration, so that the equilibrium state has been taken as the origin of potential. Unlike the kinetic energy, this functional is defined for any $\xi \in \mathcal{C}_c^\infty(\mathbb{R}^3)$ without the need of a time dependence.

Comment. Some texts like Goedbloed and Poedts (2004) derive the expression for the potential energy by imposing energy conservation, but an intuition for it can also be given. Indeed, the work done against the force \mathbf{F} on a fixed infinitesimal volume of plasma when displacing it from its equilibrium position by an amount ξ can be estimated to be $-\xi \cdot \mathbf{F}(\xi)/2$, assuming the force varies linearly over the arc length traveled, which is reasonable since the perturbation is small. Therefore, the potential energy of the whole plasma is obtained by integrating this quantity in space. Note, however, that a complex conjugation has been carried out in (2.57). This has no effect on real displacements, but it is a carefully chosen generalization to complex functions in order to ensure rich properties, such as energy conservation.

Comment. Recall that \mathbf{F} is a linearized expression for the force acting on the plasma, so the potential energy expression (2.57) holds only up to second order in ξ .

Lemma 2.10. The inner product of $\mathcal{C}_c^\infty(\mathbb{R}^3)$ is antisymmetric.

Proof. This result is immediate by using the conjugate property of the volume integral and the symmetry of the euclidean inner product:

$$\langle \xi, \eta \rangle^* = \left(\frac{1}{2} \int \rho \xi^* \cdot \eta dV \right)^* = \frac{1}{2} \int \rho (\xi^*)^* \cdot \eta^* dV = \langle \eta, \xi \rangle, \quad (2.58)$$

for any $\xi, \eta \in \mathcal{C}_c^\infty(\mathbb{R}^3)$. \square

Lemma 2.11. The kinetic energy and potential energy functionals yield real values.

Proof. It is clear that, for any perturbation trajectory, expression the kinetic energy (2.56) gives a real value. Moreover, using the antisymmetry of the inner product of $\mathcal{C}_c^\infty(\mathbb{R}^3)$, together with the self-adjointness of $\rho^{-1} \mathbf{F}$:

$$W(\xi)^* = -\langle \xi, \rho^{-1} \mathbf{F}(\xi) \rangle^* = -\langle \rho^{-1} \mathbf{F}(\xi), \xi \rangle = -\langle \xi, \rho^{-1} \mathbf{F}(\xi) \rangle = W(\xi), \quad (2.59)$$

so $W(\xi) \in \mathbb{R}$. \square

Theorem 2.12. The total plasma energy is conserved during any perturbation trajectory.

Proof. Let $\xi(r, t)$ be a perturbation trajectory. We compute the time derivative of the kinetic energy while using the time derivatives commute with the volume integrals⁶, allowing us to use the common product rule:

$$\frac{d}{dt} K(\xi) = \frac{d}{dt} \langle \dot{\xi}, \dot{\xi} \rangle = \langle \ddot{\xi}, \dot{\xi} \rangle + \langle \dot{\xi}, \ddot{\xi} \rangle = \langle \dot{\xi}, \rho^{-1} \mathbf{F}(\xi) \rangle + \langle \rho^{-1} \mathbf{F}(\xi), \dot{\xi} \rangle. \quad (2.60)$$

Recalling the self-adjointness of $\rho^{-1} \mathbf{F}$, and using the product rule once again, we get:

$$\frac{d}{dt} K(\xi) = \langle \dot{\xi}, \rho^{-1} \mathbf{F}(\xi) \rangle + \langle \xi, \rho^{-1} \mathbf{F}(\dot{\xi}) \rangle = \frac{d}{dt} \langle \xi, \rho^{-1} \mathbf{F}(\xi) \rangle = -\frac{d}{dt} W(\xi). \quad (2.61)$$

⁶This is guaranteed by the smoothness of $\xi(r, t)$.

In the previous calculation, we have used the smoothness of ξ and the Schwartz theorem to compute the time derivative of $\mathbf{F}(\xi)$ through $\mathbf{F}(\dot{\xi})$. We thus conclude the total plasma energy $K(\xi) + W(\xi)$ remains constant over time. \square

2.8 Growth rate of instabilities

In this section, we introduce the growth rate that can be associated to a given equilibrium configuration, and we will show why it is an ideal tool to understand its linear stability, as done in the literature like Linton et al. (1996) and Florido-Llinas et al. (2020).

Comment. From now on, we will let $\{\xi_n\}$ be an orthonormal set of normal modes that generate the test function space $\mathcal{C}_c^\infty(\mathbb{R}^3)$. This can be done because, as seen in Corollary 2.5, any pair of normal modes with different eigenvalue are orthogonal to each other. Furthermore, orthogonal normal modes with the same eigenvalue can be found by using the Gram-Schmidt method to obtain an orthogonal basis of the corresponding eigenspace.

Definition. The *minimal mode* is the normal mode ξ_n with a lowest corresponding value of ω_n^2 . In such case, we use the notation ξ_0 and ω_0^2 respectively.

Comment. The existence of a minimal mode will be assumed with no proof in this work, although one may study which conditions should be imposed on $\rho^{-1}\mathbf{F}$, and hence on the equilibrium quantities, to guarantee its existence. Moreover, uniqueness will be assumed in order to simplify the explanation, but the argument could be adapted to not rely on this assumption.

Comment. Recalling that a plasma configuration is unstable if there is an unstable normal mode, such condition can be rephrased as $\omega_0^2 < 0$. Hence, the problem of characterizing the stability of an equilibrium configuration is reduced to determining the sign of ω_0^2 .

Theorem 2.13. The global minimum of the potential energy functional $W : \mathcal{C}_c^\infty(\mathbb{R}^3) \rightarrow \mathbb{R}$ over all normalized test functions is ω_0^2 , and it is attained at ξ_0 :

$$W(\xi_0) = \min_{\|\xi\|=1} W(\xi) = \omega_0^2. \quad (2.62)$$

Proof. Let $\xi \in \mathcal{C}_c^\infty(\mathbb{R}^3)$ be any test functions, which can be expressed as a combination of normal modes as

$$\xi = \sum_n a_n \xi_n \quad (2.63)$$

with $a_n \in \mathbb{C}$. Then, the potential energy change due to ξ is:

$$W(\xi) = -\langle \xi, \rho^{-1}\mathbf{F}(\xi) \rangle = -\sum_{n,m} a_n^* a_m \langle \xi_n, \rho^{-1}\mathbf{F}(\xi_m) \rangle = \sum_{n,m} a_n^* a_m \omega_m^2 \langle \xi_n, \xi_m \rangle \quad (2.64)$$

$$= \sum_{n,m} a_n^* a_m \omega_m^2 \delta_{nm} = \sum_n |a_n|^2 \omega_n^2. \quad (2.65)$$

From this we obtain that $W(\xi_0) = \omega_0^2$. On the other hand, the normalization condition for ξ is

$$\|\xi\|^2 = \sum_n |a_n|^2 = 1. \quad (2.66)$$

Hence we obtain

$$W(\xi) = \sum_n |a_n|^2 \omega_n^2 \geq \omega_0^2 \sum_n |a_n|^2 = W(\xi_0), \quad (2.67)$$

which proves the desired result. This derivation was first presented in Bernstein et al. (1958), and has become fundamental to study the linear stability of ideal MHD plasmas. \square

Comment. Notice that ω_0 is also related to the potential energy of displacements that are not normalized:

$$\omega_0^2 = \min_{\|\xi\|=1} W(\xi) = \min_{\xi} W\left(\frac{\xi}{\|\xi\|}\right) = \min_{\xi} \frac{W(\xi)}{\|\xi\|^2}. \quad (2.68)$$

Definition. The *growth rate* of an unstable plasma equilibrium configuration is given by

$$\sigma = \sqrt{-\omega_0^2}. \quad (2.69)$$

which is a positive real number due to $\omega_0^2 < 0$. It is the maximum rate at which an instability can develop in time, as justified in Theorem 2.15, with help of a preliminary lemma.

Lemma 2.14. Let $I : \mathcal{C}_c^\infty(\mathbb{R}^3) \rightarrow \mathbb{R}$ be the norm squared operator,

$$I(\xi) = \frac{1}{2} \int \rho |\xi|^2 dV = \|\xi\|^2. \quad (2.70)$$

Let $I(t) = I(\xi(\cdot, t))$ be the norm squared along any perturbation trajectory. Then:

$$\ddot{I}(t) = 2K(t) - 2W(t) = 4K(t) - 2H = 2H - 4W(t). \quad (2.71)$$

Where $K(t)$ and $W(t)$ are the kinetic and potential energy, and H is the (conserved) total energy.

Proof. The proof is straightforward, starting from $I(t) = \langle \xi(t), \xi(t) \rangle$:

$$\ddot{I} = 2 \frac{d}{dt} (\langle \dot{\xi}(t), \xi(t) \rangle) = 2 (\langle \dot{\xi}(t), \dot{\xi}(t) \rangle + \langle \ddot{\xi}(t), \xi(t) \rangle) = 2K(t) - 2W(t). \quad (2.72)$$

The other equalities follow from $H = K(t) + W(t)$. \square

Definition. Let $f, g : [0, +\infty) \rightarrow \mathbb{R}$. We say that:

- ◊ $f(t)$ grows at least as $g(t)$ if there exist $k \in \mathbb{R}$ and $t_0 \geq 0$ such that $f(t) \geq kg(t)$ for all $t \geq t_0$.
- ◊ $f(t)$ grows at most as $g(t)$ if there exist $k \in \mathbb{R}$ and $t_0 \geq 0$ such that $f(t) \leq kg(t)$ for all $t \geq t_0$.
- ◊ $f(t)$ grows exactly as $g(t)$ if the two conditions above are fulfilled.

Theorem 2.15. In an unstable plasma equilibrium, the norm $\|\xi(t)\|$ grows at most as $e^{\sigma t}$. Furthermore, with appropriate initial conditions, it grows exactly as $e^{\sigma t}$.

Proof. We have seen in (2.68) that, for any $\xi \in \mathcal{C}_c^\infty(\mathbb{R}^3)$,

$$\sigma^2 \geq -\frac{W(\xi)}{I(\xi)}. \quad (2.73)$$

Hence, given a perturbation trajectory, and starting from (2.71):

$$\ddot{I}(t) = 2H - 4W(t) \leq 2H + 4\sigma^2 I(t). \quad (2.74)$$

From this follows that $I(t)$ grows at most as $e^{2\sigma t}$: although this seems intuitive, a rigorous proof is provided at the end of this chapter, in Section 2.12. Hence, there is some $k > 0$ such that

$$\|\xi(t)\|^2 \geq ke^{2\sigma t} \implies \|\xi(t)\| \geq \sqrt{k}e^{\sigma t} \quad \text{for } t \geq 0, \quad (2.75)$$

so the norm grows at most as $e^{\sigma t}$.

The trajectory which will be shown to attain such exponential growth starts with the minimal mode, and is excited with an initial velocity proportional to it:

$$\xi(0) = \xi_0, \quad \dot{\xi}(0) = \sigma \xi_0. \quad (2.76)$$

We proceed to find the (conserved) energy during the trajectory by evaluating its initial energy:

$$H = K(0) + W(0) = \sigma^2 I(\xi_0) + W(\xi_0) = \sigma^2 + \omega_0^2 = 0. \quad (2.77)$$

On the other hand, using the Cauchy-Schwartz inequality followed by (2.71):

$$\dot{I}(t)^2 = 4\langle \dot{\xi}(t), \xi(t) \rangle^2 \leq 4I(t)K(t) = I(t)\ddot{I}(t). \quad (2.78)$$

This inequality can be rearranged and integrated, recalling that $I(0) = 1$ and $\dot{I}(0) = 2\sigma$:

$$\int_0^t \frac{\dot{I}(s)}{I(s)} ds \leq \int_0^t \frac{\ddot{I}(s)}{I(s)} ds \implies \ln \frac{I(t)}{I(0)} \leq \ln \frac{\dot{I}(t)}{\dot{I}(0)} \implies \frac{\dot{I}(t)}{I(t)} \geq 2\sigma. \quad (2.79)$$

Integrating the last equation we find that $I(t) \geq I(0) e^{2\sigma t}$ and hence $\|\xi(t)\| \geq \|\xi(0)\| e^{\sigma t}$ for $t \geq 0$. This proof was originally presented in Laval et al. (1965). \square

Comment. In Section 2.2 we fixed the origin in time $t = 0$ at a time when equilibrium is being perturbed with a non-zero velocity, but still $\xi(0) = 0$. Nonetheless, there still could be a $t_0 > 0$ at which $\xi(t_0) = \xi_0$ and $\dot{\xi} = \sigma \xi_0$. In that case, an instability would continue to grow as $e^{\sigma t}$.

Comment. In a nutshell, we have introduced the concept of growth rate σ in a plasma equilibrium and we have seen in Theorem 2.15 its tight relation to the speed at which instabilities evolve in time. Furthermore, as seen in Theorem 2.13, σ can be determined via a constrained minimization of the potential energy functional over the normalized test functions of $\mathcal{C}_c^\infty(\mathbb{R}^3)$:

$$\sigma^2 = - \min_{\|\xi\|=1} W(\xi). \quad (2.80)$$

2.9 Gateaux differentiation and quadratic forms

In this section we provide some preliminary tools to tackle the minimization (2.80), in the context of calculus of variations in an arbitrary complex inner product space \mathbf{S} , such as $\mathcal{C}_c^\infty(\mathbb{R}^3)$.

Definition. Let $\varphi : \mathbf{S} \rightarrow \mathbb{R}$. The *Gateaux variation* of φ at $\xi \in \mathbf{S}$ in the direction of $\eta \in \mathbf{S}$ is

$$\delta_\eta \varphi(\xi) = \lim_{\varepsilon \rightarrow 0} \frac{\varphi(\xi + \varepsilon \eta) - \varphi(\xi)}{\varepsilon} = \frac{d}{d\varepsilon} \varphi(\xi + \varepsilon \eta) \Big|_{\varepsilon=0}, \quad (2.81)$$

whenever such limit converges; if so, we say φ is *Gateaux differentiable* at ξ . If this is the case for any $\xi \in \mathbf{S}$, we just say φ is Gateaux differentiable. As explained in Ananthasuresh (2021), this is a generalization of the directional derivatives in the finite-dimensional differential calculus.

Lemma 2.16. Let $\xi \in \mathbf{S}$ be a local extremum of $\varphi : \mathbf{S} \rightarrow \mathbb{R}$. Assume φ is Gateaux differentiable at $\xi \in \mathbf{S}$. Then, all Gateaux variations of φ at ξ vanish:

$$\delta_\eta \varphi(\xi) = 0 \quad \text{for } \eta \in \mathbf{S}. \quad (2.82)$$

In such case, we say ξ is a *stationary point* of φ .

Proof. The proof is analogous to the one for directional derivatives in differential calculus, and can be found in Ananthasuresh (2021). \square

Definition. A function $B : \mathbf{S} \times \mathbf{S} \rightarrow \mathbb{R}$ is said to be a *bilinear form* if it is conjugate linear on the first variable and linear on the second variable, i.e.

$$B\{\lambda\xi_1 + \mu\xi_2, \eta\} = \lambda^*B\{\xi_1, \eta\} + \mu^*B\{\xi_2, \eta\}, \quad (2.83)$$

$$B\{\xi, \lambda\eta_1 + \mu\eta_2\} = \lambda B\{\xi, \eta_1\} + \mu B\{\xi, \eta_2\}, \quad (2.84)$$

for any $\lambda, \mu \in \mathbb{C}$ and $\xi_i, \eta_i \in \mathbf{S}$. A bilinear form is *symmetric* if its arguments are interchangeable:

$$B\{\xi, \eta\} = B\{\eta, \xi\}, \quad (2.85)$$

for any $\xi, \eta \in \mathbf{S}$. Any inner product is an example of a symmetric bilinear form.

Definition. A function $\varphi : \mathbf{S} \rightarrow \mathbb{R}$ is said to be a *quadratic form* if there is a symmetric bilinear form $B : \mathbf{S} \times \mathbf{S} \rightarrow \mathbb{R}$ such that $\varphi(\xi) = B\{\xi, \xi\}$ for any $\xi \in \mathbf{S}$. Given a quadratic form $\varphi(\cdot)$, we will refer to its symmetric bilinear form as $\varphi\{\cdot, \cdot\}$. For example, the norm squared $I(\xi) = \|\xi\|^2$ is a quadratic form with the dot product $I\{\xi, \eta\} = \langle \xi, \eta \rangle$ as a symmetric bilinear form. Any linear combination of quadratic forms is also a quadratic form.

Lemma 2.17. The potential energy $W : \mathcal{C}_c^\infty(\mathbb{R}^3) \rightarrow \mathbb{R}$ is a quadratic form in the inner product space of test functions.

Proof. We define the symmetric bilinear form candidate

$$W\{\xi, \eta\} = -\langle \xi, \rho^{-1}\mathbf{F}(\eta) \rangle \quad \text{for } \xi, \eta \in \mathcal{C}_c^\infty(\mathbb{R}^3). \quad (2.86)$$

Indeed, the potential energy operator was defined in (2.57) as $W(\xi) = -\langle \xi, \rho^{-1}\mathbf{F}(\xi) \rangle = W\{\xi, \xi\}$. The bilinearity follows automatically from the bilinearity of the inner product and the linearity of $\rho^{-1}\mathbf{F}$. Finally, we can prove the symmetry of $W\{\cdot, \cdot\}$ by using self-adjointness of $\rho^{-1}\mathbf{F}$:

$$W\{\xi, \eta\} = -\langle \xi, \rho^{-1}\mathbf{F}(\eta) \rangle = -\langle \rho^{-1}\mathbf{F}(\xi), \eta \rangle = -\langle \eta, \rho^{-1}\mathbf{F}(\xi) \rangle = W\{\eta, \xi\}. \quad (2.87)$$

In conclusion, $W\{\cdot, \cdot\}$ is a symmetric bilinear form, making $W(\cdot)$ a quadratic form. \square

Lemma 2.18. Any quadratic form $\varphi : \mathbf{S} \rightarrow \mathbb{R}$ is Gateaux differentiable, and its Gateaux variation at $\xi \in \mathbf{S}$ in the direction $\eta \in \mathbf{S}$ is given by

$$\delta_\eta \varphi(\xi) = 2\varphi\{\xi, \eta\}. \quad (2.88)$$

Proof. Let $\varepsilon > 0$ and $\eta \in \mathbf{S}$. Expanding the bilinear form φ :

$$\varphi(\xi + \varepsilon\eta) = \varphi(\xi) + 2\varepsilon\varphi\{\xi, \eta\} + \varepsilon^2\varphi(\eta). \quad (2.89)$$

Therefore, the Gateaux variation of φ in the direction η is

$$\delta_\eta \varphi(\xi) = \frac{d}{d\varepsilon} \varphi(\xi + \varepsilon\eta) \Big|_{\varepsilon=0} = 2\varphi\{\xi, \eta\}, \quad (2.90)$$

as we wanted to prove. \square

2.10 Determination of the growth rate

In this section we make further steps towards the constrained minimization of the potential energy functional, in a view to determine the growth rate σ corresponding to a plasma equilibrium.

Comment. When studying plasma stability, it is common to fix the boundary conditions of the displacements $\xi : \Omega \subset \mathbb{R}^3 \rightarrow \mathbb{C}^3$ through

$$\xi|_{\partial\Omega} = h, \quad \text{for } h : \partial\Omega \rightarrow \mathbb{C}^3, \quad (2.91)$$

where h is continuous over $\partial\Omega$. The boundary conditions vary depending on the context of the stability analysis being carried out.

Definition. Let $\Omega \subset \mathbb{R}^n$ be an open bounded subset with a smooth boundary $\partial\Omega$. Consider $f, g : \Omega \times \mathbb{R}^m \times \mathbb{R}^{n \times m} \rightarrow \mathbb{R}$ to be C^1 functions, and the functionals $\mathcal{F}, \mathcal{G} : C^1(\bar{\Omega}; \mathbb{R}^m) \rightarrow \mathbb{R}$ given by

$$\mathcal{F}(\xi) = \int_{\Omega} f(r, \xi(r), D\xi(r)) dV, \quad \mathcal{G}(\xi) = \int_{\Omega} g(r, \xi(r), D\xi(r)) dV. \quad (2.92)$$

An *isoperimetric problem*⁷ seeks the local minima of \mathcal{F} over the class of admissible functions \mathcal{A} , consisting in functions normalized through \mathcal{G} and satisfying a continuous boundary condition h :

$$\mathcal{A} = \{\xi \in C^1(\bar{\Omega}; \mathbb{R}^m) \text{ such that } \mathcal{G}(\xi) = 1 \text{ and } \xi|_{\partial\Omega} = h\}. \quad (2.93)$$

Comment. A very common approach to isoperimetric problems consists in using Lagrange multipliers, which help transform a constrained minimization problem into the optimization of a new function which is free of constraints, as can be seen in the following result.

Lagrange multiplier rule for variational problems. Let ξ_0 be a solution to the isoperimetric problem defined above. Assume there exists $\eta \in C_c^\infty(\Omega; \mathbb{R}^m)$ such that $\delta_\eta \varphi(\xi_0) \neq 0$. Then, there exists a Lagrange multiplier $\lambda \in \mathbb{R}$ such that ξ_0 is a stationary point of the functional $\mathcal{U} : C^1(\bar{\Omega}; \mathbb{R}^m) \rightarrow \mathbb{R}$ defined as

$$\mathcal{U}(\xi) = \mathcal{F}(\xi) + \lambda \mathcal{G}(\xi). \quad (2.94)$$

Extracted from page 53 of the magnificent [Cristoferi \(2016\)](#).

We will use a slightly different version of this result, where $\Omega = \mathbb{R}^n$ instead of a bounded set, and we consider smooth complex functions with compact support $\xi \in C_c^\infty(\Omega; \mathbb{C}^m)$, such that the boundary condition for ξ is to vanish at infinity. The proof of this version will not be covered, but it should be very similar to the proof of the preceding result.

Theorem 2.19. The minimal mode ξ_0 is a stationary point of the *generalized energy* functional $U : C_c^\infty(\mathbb{R}^3) \rightarrow \mathbb{R}$, which is given by

$$U(\xi) = W(\xi) + \lambda I(\xi), \quad (2.95)$$

where the Lagrange multiplier is related to the growth rate via $\lambda = \sigma^2$.

Proof. We start by using the Lagrange multiplier rule, letting $\mathcal{F} = W$ be the potential energy and $\mathcal{G} = I$ the norm squared functional. We take ξ_0 to be the minimal mode, since it is a local (in fact, global) minimum of W constrained to $I(\xi) = 1$, and satisfying our boundary condition of vanishing at infinity. Furthermore, applying this result requires verifying the hypothesis that there exists a $\eta \in C_c^\infty(\mathbb{R}^3)$ such that $\delta_\eta I(\xi_0) \neq 0$. Indeed, letting $\eta = \xi_0$, and using the expression for

⁷This is due to the famous mathematical problem of finding the shape of the closed plane curve which, fixing the perimeter, maximizes the area enclosed in it.

the Gateaux variation of a quadratic form (2.88) we get

$$\delta_{\boldsymbol{\eta}} I(\boldsymbol{\xi}_0) = 2I\{\boldsymbol{\xi}_0, \boldsymbol{\eta}\} = 2I(\boldsymbol{\xi}_0) = 2 \neq 0. \quad (2.96)$$

Hence, there exists a Lagrange multiplier λ such that $\boldsymbol{\xi}_0$ is a stationary point of the functional $U(\boldsymbol{\xi}) = W(\boldsymbol{\xi}) + \lambda I(\boldsymbol{\xi})$, so that

$$\delta_{\boldsymbol{\eta}} U(\boldsymbol{\xi}_0) = 0 \quad \text{for } \boldsymbol{\eta} \in \mathcal{C}_c^\infty(\mathbb{R}^3). \quad (2.97)$$

We recall U is a quadratic form in $\mathcal{C}_c^\infty(\mathbb{R}^3)$, since it is a linear combination of quadratic forms. Then, letting $\boldsymbol{\eta} = \boldsymbol{\xi}_0$:

$$\delta_{\boldsymbol{\eta}} U(\boldsymbol{\xi}_0) = 2U\{\boldsymbol{\xi}_0, \boldsymbol{\eta}\} = 2U(\boldsymbol{\xi}_0) = 2(W(\boldsymbol{\xi}_0) + \lambda I(\boldsymbol{\xi}_0)) = 2(-\sigma^2 + \lambda) = 0, \quad (2.98)$$

yielding $\lambda = \sigma^2$ as desired. \square

Comment. Although the minimal mode $\boldsymbol{\xi}_0$ satisfies a sufficient condition for being a local minimum of U it has not been discussed whether this is the case or not, and it should not be relevant for the application of this method. However, it can easily proven that it is never a local maximum. Indeed, the second-order Gateaux variation of U in the directions $\boldsymbol{\eta}_1, \boldsymbol{\eta}_2 \in \mathcal{C}_c^\infty(\mathbb{R}^3)$ is given by

$$\delta_{\boldsymbol{\eta}_1 \boldsymbol{\eta}_2} U(\boldsymbol{\xi}) = \delta_{\boldsymbol{\eta}_1} (\delta_{\boldsymbol{\eta}_2} U(\boldsymbol{\xi})) = \frac{d}{d\varepsilon} 2U\{\boldsymbol{\xi}, \boldsymbol{\eta}_2\} \Big|_{\varepsilon=0} = 2U\{\boldsymbol{\eta}_1, \boldsymbol{\eta}_2\}. \quad (2.99)$$

As expected from the finite dimensional case, the second-order differentiation of a quadratic form yields a constant function of $\boldsymbol{\xi}$. Letting both directions be the same, $\boldsymbol{\eta}_1 = \boldsymbol{\eta}_2 = \boldsymbol{\eta}$, we get

$$\delta_{\boldsymbol{\eta}_1 \boldsymbol{\eta}_2} U = 2U(\boldsymbol{\eta}) = 2(W(\boldsymbol{\eta}) + \sigma^2 I(\boldsymbol{\eta})) = 2I(\boldsymbol{\eta}) \left(\frac{W(\boldsymbol{\eta})}{I(\boldsymbol{\eta})} + \sigma^2 \right) \geq 0, \quad (2.100)$$

which is incompatible with U having any local maxima. \square

Comment. The generalized energy may have more than one stationary point. If a minimal mode needs to be determined, one can evaluate at each normalized stationary point of U , and choose one that gives the smallest value.

Comment. The Lagrange multiplier, and thus the growth rate σ , can be determined algebraically by finding the stationary points of U and then imposing the boundary conditions. In Chapter 3 we provide an example of this analysis for a plasma equilibrium with a cylindrical geometry.

2.11 Potential energy for incompressible displacements

The problem of minimizing the generalized energy functional U still seems very complex due to the cumbersome expression of W in terms of the displacement $\boldsymbol{\xi}$. Lemma 2.20 will help us in this endeavor.

Comment. First, we recall from Chapter 1 that, due to the continuity equation (1.7), incompressible fluids are the ones satisfying $\nabla \cdot \mathbf{v} = 0$. In the case of a static equilibria being displaced, this means

$$\nabla \cdot \frac{\partial \boldsymbol{\xi}}{\partial t} = \frac{\partial}{\partial t} (\nabla \cdot \boldsymbol{\xi}) = 0. \quad (2.101)$$

Recalling that trajectories satisfy $\boldsymbol{\xi}(\mathbf{r}, 0) = 0$, the previous equation can be integrated in time to give the condition $\nabla \cdot \boldsymbol{\xi} = 0$.

Definition. A displacement $\boldsymbol{\xi} \in \mathcal{C}_c^\infty(\mathbb{R}^3)$ is said to be *incompressible* if

$$\nabla \cdot \boldsymbol{\xi} = 0. \quad (2.102)$$

Lemma 2.20. The following expression holds for the potential energy functional:

$$W(\boldsymbol{\xi}) = \frac{1}{2} \int \left[\frac{|\boldsymbol{Q}|^2}{\mu_0} - \boldsymbol{\xi}^* \cdot (\boldsymbol{J} \times \boldsymbol{Q}) + \boldsymbol{\xi}^* \cdot \nabla p (\nabla \cdot \boldsymbol{\xi}) + \gamma p (\nabla \cdot \boldsymbol{\xi})^2 \right] dV \quad (2.103)$$

Furthermore, the most unstable displacements are incompressible, that is, $\nabla \cdot \boldsymbol{\xi} = 0$. Hence, the stability analysis is unaltered by considering only incompressible displacements, and using the expression:

$$W(\boldsymbol{\xi}) = \frac{1}{2\mu_0} \int (|\boldsymbol{Q}|^2 - \boldsymbol{\xi}^* \cdot (\nabla \times \boldsymbol{B}) \times \boldsymbol{Q}) dV \quad (2.104)$$

Proof. It consists in developing the expression of W and applying integral theorems, and can be found in several text books such as [Priest \(2013\)](#). An alternate derivation, which is quite interesting from the physics point of view since it starts from expression (1.16) for the potential energy, can also be found in [Nishikawa and Wakatani \(2000\)](#). \square

2.12 Differential inequality with exponential growth

This section is auxiliary for the proof of Theorem 2.15.

Lemma 2.21. Let $y : [0, +\infty) \rightarrow \mathbb{R}$ be a smooth function which satisfies the homogeneous differential inequality

$$\ddot{y}(t) \leq \alpha^2 y(t) \quad \text{for } t \geq 0, \quad (2.105)$$

for some $\alpha > 0$. Then, $y(t)$ grows at most as $e^{\alpha t}$.

Proof. We introduce the change of variable

$$z(t) = \ln y(t) - \alpha t. \quad (2.106)$$

If we show that z is bounded by some value $Z \in \mathbb{R}$, then it will follow that

$$y(t) \leq (e^Z)^{e^{\alpha t}} \quad \text{for } t \geq 0, \quad (2.107)$$

and the proof will be done. We thus proceed to compute the derivatives of z :

$$\dot{z}(t) = \frac{\dot{y}(t)}{y(t)} - \alpha, \quad \ddot{z}(t) = \frac{\ddot{y}(t)}{y(t)} - \frac{\dot{y}(t)^2}{y(t)^2} \quad (2.108)$$

Using the hypothesis (2.105), one can reach a differential inequality involving only z , which can be recast and integrated:

$$\ddot{z} + (\dot{z} + \alpha)^2 \leq \alpha^2 \implies \frac{\ddot{z}}{\dot{z}} + \dot{z} \leq -2\alpha \implies \ln \dot{z} + z \leq c_1 - 2\alpha t, \quad (2.109)$$

being $c_1 \in \mathbb{R}$ a constant. Note that $\ln \dot{z} + z = \ln (\dot{z} e^z)$, so the previous relation can be exponentiated and integrated once more:

$$\dot{z} e^z \leq e^{c_1 - 2\alpha t} \implies e^z \leq c_2 - \frac{1}{2\alpha} e^{c_1 - 2\alpha t} \leq c_2 \quad (2.110)$$

for some $c_2 \in \mathbb{R}$. Hence, z is bounded by $Z = \ln c_2$. \square

Corollary 2.22. Let $I : [0, +\infty) \rightarrow \mathbb{R}$ be a smooth function which satisfies the differential inequality

$$\ddot{I}(t) \leq 4\sigma^2 I(t) + 2H \quad \text{for } t \geq 0, \quad (2.111)$$

where $\sigma > 0$ and $H \in \mathbb{R}$. Then, $I(t)$ grows at least as $e^{2\sigma t}$.

Proof. The non-homogeneous inequality (2.111) can be transformed into an homogeneous one by a simple change of variable,

$$y(t) = I(t) + \frac{H}{2\sigma^2}, \quad (2.112)$$

which leads to

$$\ddot{y} \leq (2\sigma)^2 y \quad \text{for } t \geq 0. \quad (2.113)$$

Using Lemma 2.21, there exists $k \in \mathbb{R}$ such that $y(t) \leq ke^{2\sigma t}$ for $t \geq 0$. Then:

$$I(t) = y(t) - \frac{H}{2\sigma^2} \leq ke^{2\sigma t} + \frac{|H|}{2\sigma^2} \leq \left(k + \frac{|H|}{2\sigma^2} \right) e^{2\sigma t}, \quad (2.114)$$

which proves the desired result. \square

3 . Cylindrical Plasma Stability

3.1 Magnetic flux ropes as cylindrical plasmas

In this section we continue to develop the growth rate method by adapting it to a cylindrical plasma with a boundary that is free to move, so it can be applied to the study of instabilities in heliospheric MFRs. Starting from the baseline method in Linton et al. (1996), which focuses on the kink instability of twisted flux tubes, we generalize it by considering a more general set of plasma instabilities and an arbitrary radial density profile.

The first step in this analysis is to consider a plasma structure with cylindrical symmetry. Such an assumption starts from the intuition of carrying out a local approximation of the flux ropes in CMEs, which usually have rather toroidal shapes with the ends connected to the surface of the Sun, as illustrated in Figure 3.1. Moreover, cylindrical models have recently been used to fit MFRs (see Nieves-Chinchilla et al. (2016)) and study their stability (Florido-Llinas et al. (2020)). Indeed, it is common to carry out a simplified analysis which can later be further explored by making more realistic assumptions, such as using a more complex but appropriate geometry.

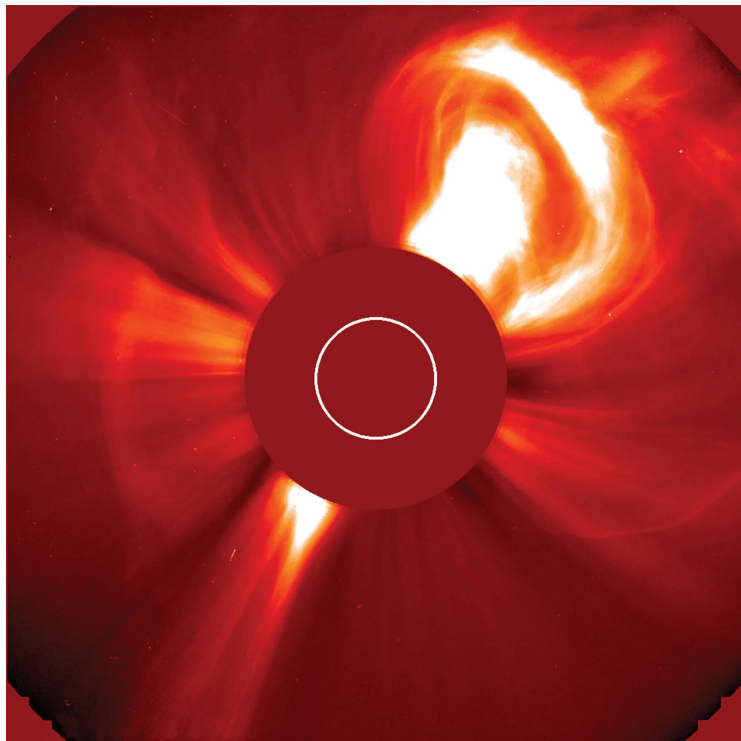


Figure 3.1: Image of a coronal mass ejection, taken from the Solar and Heliospheric Observatory (SOHO, ESA/NASA) on December, 2002. Captured using a coronagraph, which blocks the solar disc in order to sense the light emitted from the corona. [Source](#).

Hence, during the following sections, we consider a plasma volume V , which is a cylindrical shell of length L , inner radius a and outer radius b , with $0 \leq a < b \leq +\infty$. This geometry will be of use to simultaneously study the interior of the flux rope, setting $[a, b] = [0, R]$, and its exterior, with $[a, b] = [R, +\infty]$, being R the radius of the structure.

We also consider the plasma equilibrium configuration has cylindrical symmetry, i.e. both rotational and axial symmetry. The latter can be justified by considering the cylinder is long compared to its cross section. As seen previously, an ideal MHD plasma equilibrium is characterized by the quantities \mathbf{B}, p, ρ . We can now proceed to discuss the equilibrium variables in a cylindrical plasma, under the only assumption of cylindrical symmetry.

Lemma 3.1. The general expression for a cylindrically symmetrical magnetic field configuration \mathbf{B} is given by $\mathbf{B}(r) = (0, B_\theta(r), B_z(r))$.

Proof. If \mathbf{B} has cylindrical symmetry, it cannot have any dependence on θ and z , so it can be expressed as $\mathbf{B}(r) = (B_r(r), B_\theta(r), B_z(r))$. Recalling the expression for the divergence in cylindrical coordinates

$$\nabla \cdot \mathbf{B} = \frac{1}{r} \frac{\partial(rB_r)}{\partial r} + \frac{1}{r} \frac{\partial B_\theta}{\partial \theta} + \frac{\partial B_z}{\partial z}, \quad (3.1)$$

the divergence-free condition becomes a first order differential equation:

$$\frac{dB_r}{dr} + \frac{B_r}{r} = 0. \quad (3.2)$$

Its general solution is $B_r(r) = C/r$, for some constant $C \in \mathbb{R}$. The magnetic field cannot be unbounded at the cylinder axis, so $C = 0$, and thus $\mathbf{B}(r) = (0, B_\theta(r), B_z(r))$. \square

For now, no more assumptions will be made on the equilibrium magnetic field: the modeling of the magnetic field will be covered in Chapter 4.

On the other hand, the pressure profile will not be used, since it does not play a key role in the stability analysis developed in Chapter 2. However, we should be mindful that it is determined up to a constant by the magnetic field, as previously discussed in Section 2.2:

$$\nabla p = \mathbf{J} \times \mathbf{B} \quad (3.3)$$

where \mathbf{J} is given in terms of \mathbf{B} through Ampere's law.

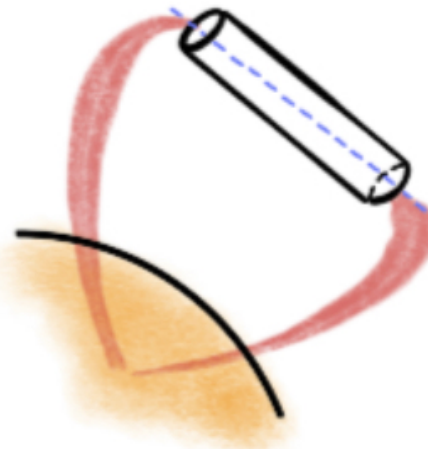


Figure 3.2: Cylindrical approximation of the MFR of a CME. Art by Marta Florido.

Regarding the equilibrium density ρ , in Linton et al. (1996) and Florido-Llinas et al. (2020) it is assumed to be constant everywhere. However, spacecraft data shows that MFRs have a variable density profile, so future stability studies need to be able to account for more complex density distributions. For this reason, the theoretical background of this method will continue to be developed for an arbitrary radial density $\rho(r)$. Nonetheless, a constant density will be assumed after Section 3.6 in a view to simplify the analysis.

3.2 Fourier perturbation analysis

A key first step to determine the growth rate corresponding to a plasma equilibrium configuration, is consider displacements of the form

$$\xi(r, \theta, z) = (\xi_r(r), \xi_\theta(r), \xi_z(r)) e^{i(m\theta + kz)}, \quad (3.4)$$

where $m \in \mathbb{Z}$ and $k \in \mathbb{R}$ are the azimuthal and axial wave numbers, respectively. This way, we restrict the optimization of the generalized energy U to a subset of the space of test functions, which really simplifies the calculations. There is really no formal justification for this assumption, but it is by far the most popular approach to tackle plasma stability in cylindrical systems, as can be seen in several publications and textbooks (for instance, see Freidberg (2007), Priest (2013)).

Nevertheless, an intuition for it can be sought using Fourier analysis. Using the axial symmetry in z , as well as the rotational symmetry in z , any displacement ξ satisfying the appropriate Dirichlet conditions can be expanded as a Fourier transform in z and a Fourier series in θ :

$$\xi(r, \theta, z) = \sum_{m=-\infty}^{+\infty} \int_{-\infty}^{+\infty} dk \xi_{mk}(r) e^{i(m\theta + kz)} \quad (3.5)$$

Then, assuming perturbations of the form (3.4) can be thought of as analyzing one Fourier harmonic at a time.

One of the key features of this approach is that each value of the azimuthal wave number m yields a class of displacements with a different geometrical interpretation. Hence, we often refer to m as the *order* of the instability. Some key examples are the following (Gsporer (2009)):

- ◊ *Sausage instability* ($m = 0$): the lack of angular dependence creates a displacement which conserves the a circular cross-section, with a radius that oscillates with z .
- ◊ *Kink instability* ($m = 1$): its angular dependence causes the cylinder become a helix itself.
- ◊ Filamentation mode ($m = 2$): the cross-section is displaced towards an elliptical shape.
- ◊ Filamentation mode ($m = 3$): the cross-section is displaced towards a pear-like shape.

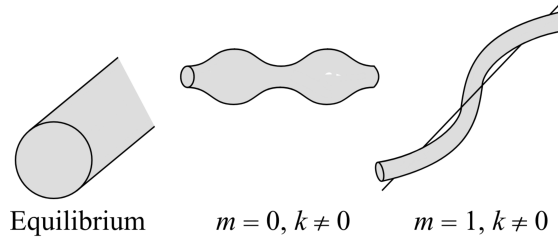


Figure 3.3: Sketch of the sausage and kink instability. Extracted from Freidberg (2007).

In general, higher values of m lead to more complex cross-section distortions. Note that negative values of m are also aloud, inverting the angular dependence, but yielding a very similar behavior. For example, $m = -1$ corresponds to the kink instability with an inverted chirality. In fact, it is deduced from (3.4) that the displacements with wave numbers (m, k) and $(-m, -k)$ are totally equivalent up to a translation in space.

The development of an MHD stability analysis of a cylindrical plasma system under perturbations of this type was first studied in [Newcomb \(1960\)](#), via the application of the Energy Principle by [Bernstein et al. \(1958\)](#). One of Newcomb's key conclusions was the following result:

Instability comparison theorem. The displacements which lead to a greater decrease in the potential energy with respect to the equilibrium configuration are those with $|m| = 1$. Hence, if a linear pinch is stable for $m = 1$ and $k \in \mathbb{R}$, it must also be stable for all values of m . [Newcomb \(1960\)](#).

The previous theorem is based on the traditional definition of stability, where any perturbation which decreases the potential energy of the system in equilibrium is regarded as unstable. However, [Goedbloed \(1974\)](#) introduced a more modern and practical definition for stability, called σ -stability, which is also more restrictive. An equilibrium is said to be σ -stable if all the instabilities grow at most as $e^{\sigma t}$, where $\sigma > 0$ is fixed.

Indeed, a growth rate analysis can find instabilities with very slowly growing exponential growths with a time constant that can be way larger than the time scale of the system being considered. Such a situation can be classified as σ -stable by fixing a sufficiently large σ . In Chapter 4, we will use the methods developed during the following sections to evaluate the applicability of Newcomb's comparison theorem to this new conception of stability: are the kink modes $m = 1$ the most σ -stable?

Finally, we will also assume the perturbation displacements are incompressible. This is a legitimate assumption, taking into account Lemma 2.20. Note that the incompressibility condition $\nabla \cdot \xi = 0$ can be expressed in cylindrical coordinates as:

$$\nabla \cdot \xi = \frac{1}{r} \frac{d(r\xi_r)}{dr} + i \frac{m}{r} \xi_\theta + ik\xi_z = 0. \quad (3.6)$$

Lemma 3.2. Consider the perturbation displacement in cylindrical coordinates,

$$\xi(r, \theta, z) = (\xi_r(r), \xi_\theta(r), \xi_z(r)) e^{i(m\theta + kz)}. \quad (3.7)$$

We assume the phase of each component of ξ does not change with r , and that the functions $|\xi_\theta|$ and $r|\xi_z|$ are linearly independent. Then, we can take ξ_r to be a real function of r , and the components ξ_θ, ξ_z to be imaginary. In particular,

$$|\xi|^2 = (\xi_r)^2 + (i\xi_\theta)^2 + (i\xi_z)^2. \quad (3.8)$$

Proof. Without loss of generality, we can take $\xi_r \in \mathbb{R}$, since a global phase does not affect the calculations that will be made in the rest of this work. Then, incompressibility (3.6) leads to the condition

$$\Re\left(\frac{m}{r}\xi_\theta + k\xi_z\right) = \frac{m}{r}|\xi_\theta|\cos\varphi_\theta + k|\xi_z|\cos\varphi_z = 0, \quad (3.9)$$

where \Re notes the real part and φ denotes the phase of each component. Multiplying the equation by r , the linear independence condition yields $\cos\varphi_\theta = \cos\varphi_z = 0$, so ξ_θ and ξ_z are imaginary. \square

3.3 Expansion of the generalized energy

The aim of this section is to, given the equilibrium quantities, obtain the generalized energy U as a functional of a general cylindrical perturbation displacement, given in cylindrical coordinates by

$$\xi(r, \theta, z) = (\xi_r(r), \xi_\theta(r), \xi_z(r)) e^{i(m\theta + kz)} = \tilde{\xi}(r) e^{i(m\theta + kz)}, \quad (3.10)$$

and with an equilibrium magnetic field given by

$$\mathbf{B}(r) = (0, B_\theta(r), B_z(r)) \quad (3.11)$$

The equations obtained will be a generalization of the ones in Linton et al. (1996). We start by finding a suitable expression for the perturbed magnetic field $\mathbf{Q} = \nabla \times (\boldsymbol{\xi} \times \mathbf{B})$.

Lemma 3.3. The perturbed magnetic field is given by

$$\mathbf{Q} = \left(iF\tilde{\boldsymbol{\xi}} - r \frac{d}{dr} \left(\frac{B_\theta}{r} \right) \boldsymbol{\xi}_r \hat{\boldsymbol{\theta}} - \frac{dB_z}{dr} \boldsymbol{\xi}_r \hat{\mathbf{z}} \right) e^{i(m\theta+kz)} \quad (3.12)$$

where we define

$$F = \frac{m}{r} B_\theta + kB_z. \quad (3.13)$$

Proof. Notice that, using the well known vector calculus identity

$$\mathbf{Q} = \nabla \times (\boldsymbol{\xi} \times \mathbf{B}) = (\nabla \cdot \mathbf{B}) \boldsymbol{\xi} - (\nabla \cdot \boldsymbol{\xi}) \mathbf{B} + (\mathbf{B} \cdot \nabla) \boldsymbol{\xi} - (\boldsymbol{\xi} \cdot \nabla) \mathbf{B}, \quad (3.14)$$

added to Gauss' law $\nabla \cdot \mathbf{B} = 0$ and the incompressibility condition $\nabla \cdot \boldsymbol{\xi} = 0$, yields

$$\mathbf{Q} = (\mathbf{B} \cdot \nabla) \boldsymbol{\xi} - (\boldsymbol{\xi} \cdot \nabla) \mathbf{B}. \quad (3.15)$$

These terms can be computed using the following expression for general vector fields given in cylindrical coordinates by $\mathbf{A} = (A_r, A_\theta, A_z)$ and $\mathbf{B} = (B_r, B_\theta, B_z)$:

$$(\mathbf{A} \cdot \nabla) \mathbf{B} = A_r \frac{\partial \mathbf{B}}{\partial r} + \frac{A_\theta}{r} \frac{\partial \mathbf{B}}{\partial \theta} + A_z \frac{\partial \mathbf{B}}{\partial z} - \frac{1}{r} A_\theta B_\theta \hat{\mathbf{r}} + \frac{1}{r} A_\theta B_r \hat{\boldsymbol{\theta}}. \quad (3.16)$$

We thus proceed to compute

$$\begin{aligned} (\mathbf{B} \cdot \nabla) \boldsymbol{\xi} &= \frac{B_\theta}{r} \frac{\partial \boldsymbol{\xi}}{\partial \theta} + B_z \frac{\partial \boldsymbol{\xi}}{\partial z} - \frac{1}{r} B_\theta \boldsymbol{\xi}_\theta e^{i(m\theta+kz)} \hat{\mathbf{r}} + \frac{1}{r} B_\theta \boldsymbol{\xi}_r e^{i(m\theta+kz)} \hat{\boldsymbol{\theta}} \\ &= \left(i \frac{m}{r} B_\theta \tilde{\boldsymbol{\xi}} + ik B_z \tilde{\boldsymbol{\xi}} - \frac{1}{r} B_\theta \boldsymbol{\xi}_\theta \hat{\mathbf{r}} + \frac{1}{r} B_\theta \boldsymbol{\xi}_r \hat{\boldsymbol{\theta}} \right) e^{i(m\theta+kz)} \end{aligned} \quad (3.17)$$

and

$$(\boldsymbol{\xi} \cdot \nabla) \mathbf{B} = \left(\boldsymbol{\xi}_r \frac{\partial \mathbf{B}}{\partial r} - \frac{1}{r} B_\theta \boldsymbol{\xi}_\theta \hat{\mathbf{r}} \right) e^{i(m\theta+kz)} \quad (3.18)$$

which lead to the desired result

$$\mathbf{Q} = \left(iF\tilde{\boldsymbol{\xi}} - \left(\frac{dB_\theta}{dr} - \frac{B_\theta}{r} \right) \boldsymbol{\xi}_r \hat{\boldsymbol{\theta}} - \frac{dB_z}{dr} \boldsymbol{\xi}_r \hat{\mathbf{z}} \right) e^{i(m\theta+kz)}. \quad (3.19)$$

Note that an alternative expression for \mathbf{Q} can also be found using its definition instead of vector calculus identities, but result (3.12) ends up being more convenient. \square

Lemma 3.4. The generalized energy can be expressed in terms of the displacement components through the integral expression

$$U(\boldsymbol{\xi}_r, \boldsymbol{\xi}_\theta, \boldsymbol{\xi}_z) = \frac{\pi L}{\mu_0} \int_a^b \left(r (F^2 + \lambda\rho) |\boldsymbol{\xi}|^2 + 4iFB_\theta \boldsymbol{\xi}_r \boldsymbol{\xi}_\theta + \Theta \boldsymbol{\xi}_r^2 \right) dr, \quad (3.20)$$

where the following parameter has been conveniently defined:

$$\Theta = \frac{2B_\theta^2}{r} - \frac{dB_\theta^2}{dr}.$$

Proof. The potential energy and norm are given by

$$W(\boldsymbol{\xi}) = \frac{1}{2\mu_0} \int_V (|\boldsymbol{Q}|^2 - \boldsymbol{\xi}^* \cdot (\nabla \times \boldsymbol{B}) \times \boldsymbol{Q}) dV, \quad I(\boldsymbol{\xi}) = \frac{1}{2\mu_0} \int_V \rho |\boldsymbol{\xi}|^2 dV. \quad (3.21)$$

Hence, the generalized energy is given by

$$U(\boldsymbol{\xi}) = W(\boldsymbol{\xi}) + \lambda I(\boldsymbol{\xi}) = \frac{1}{2\mu_0} \int_V (|\boldsymbol{Q}|^2 - \boldsymbol{\xi}^* \cdot (\nabla \times \boldsymbol{B}) \times \boldsymbol{Q} + \lambda \rho |\boldsymbol{\xi}|^2) dV. \quad (3.22)$$

Note that Lemma 3.3 shows that \boldsymbol{Q} can be expressed as

$$\boldsymbol{Q}(r, \theta, z) = \tilde{\boldsymbol{Q}}(r) e^{i(m\theta + kz)}, \quad (3.23)$$

so that the θ and z dependence of the three terms in equation (3.22) vanishes, and the whole integrand is only a function of r . Thus, we integrate over the cylinder as

$$\int_V u(r) dV = \int_a^b r u(r) dr \int_0^{2\pi} d\theta \int_0^L dz = 2\pi L \int_a^b r u(r) dr, \quad (3.24)$$

which leads to

$$U(\boldsymbol{\xi}) = \frac{\pi L}{\mu_0} \int_a^b r (|\boldsymbol{Q}|^2 - \boldsymbol{\xi}^* \cdot (\nabla \times \boldsymbol{B}) \times \boldsymbol{Q} + \lambda \rho |\boldsymbol{\xi}|^2) dr. \quad (3.25)$$

We must now expand each of the three terms in the integral in terms of ξ_r , ξ_θ and ξ_z . The third term can be found immediately using Lemma 3.2. We now compute the first term by expanding $|\boldsymbol{Q}|^2$ starting from (3.12):

$$\begin{aligned} |\boldsymbol{Q}|^2 &= \boldsymbol{Q}^* \cdot \boldsymbol{Q} = \left(-iF\tilde{\boldsymbol{\xi}}^* - r \frac{d}{dr} \left(\frac{B_\theta}{r} \right) \xi_r \hat{\boldsymbol{\theta}} - \frac{dB_z}{dr} \xi_r \hat{\boldsymbol{z}} \right) \cdot \left(iF\tilde{\boldsymbol{\xi}} - r \frac{d}{dr} \left(\frac{B_\theta}{r} \right) \xi_r \hat{\boldsymbol{\theta}} - \frac{dB_z}{dr} \xi_r \hat{\boldsymbol{z}} \right) \\ &= F^2 |\boldsymbol{\xi}|^2 - 2iF\xi_r \left(r \frac{d}{dr} \left(\frac{B_\theta}{r} \right) \xi_\theta + \frac{dB_z}{dr} \xi_z \right) + \xi_r^2 \left(\left(\frac{dB_z}{dr} \right)^2 + \left(r \frac{d}{dr} \left(\frac{B_\theta}{r} \right) \right)^2 \right). \end{aligned} \quad (3.26)$$

In order to evaluate the second term in the integral, we start by computing the curl of \boldsymbol{B} in cylindrical coordinates:

$$\nabla \times \boldsymbol{B} = \frac{1}{r} \begin{vmatrix} \hat{\boldsymbol{r}} & r\hat{\boldsymbol{\theta}} & \hat{\boldsymbol{z}} \\ \partial_r & \partial_\theta & \partial_z \\ B_r & rB_\theta & B_z \end{vmatrix} = \frac{1}{r} \begin{vmatrix} \hat{\boldsymbol{r}} & r\hat{\boldsymbol{\theta}} & \hat{\boldsymbol{z}} \\ d_r & 0 & 0 \\ 0 & rB_\theta & B_z \end{vmatrix} = -\frac{dB_z}{dr} \hat{\boldsymbol{\theta}} + \frac{1}{r} \frac{d}{dr} (rB_\theta) \hat{\boldsymbol{z}}. \quad (3.27)$$

Now, we proceed to evaluate:

$$\begin{aligned} -\boldsymbol{\xi}^* \cdot (\nabla \times \boldsymbol{B}) \times \boldsymbol{Q} &= -\tilde{\boldsymbol{\xi}}^* \cdot \left(-\frac{dB_z}{dr} \hat{\boldsymbol{\theta}} + \frac{1}{r} \frac{d}{dr} (rB_\theta) \hat{\boldsymbol{z}} \right) \times \left(iF\tilde{\boldsymbol{\xi}} - r \frac{d}{dr} \left(\frac{B_\theta}{r} \right) \xi_r \hat{\boldsymbol{\theta}} - \frac{dB_z}{dr} \xi_r \hat{\boldsymbol{z}} \right) \\ &= 2iF\xi_r \left(\frac{dB_z}{dr} \xi_z + \frac{1}{r} \frac{d}{dr} (rB_\theta) \xi_\theta \right) - \xi_r^2 \left(\left(\frac{dB_z}{dr} \right)^2 + \frac{d}{dr} (rB_\theta) \frac{d}{dr} \left(\frac{B_\theta}{r} \right) \right). \end{aligned} \quad (3.28)$$

In the last calculation, the following triple products have been performed:

$$\tilde{\boldsymbol{\xi}}^* \cdot (\hat{\boldsymbol{\theta}} \times \tilde{\boldsymbol{\xi}}) = \begin{vmatrix} \xi_r & -\xi_\theta & -\xi_z \\ 0 & 1 & 0 \\ \xi_r & \xi_\theta & \xi_z \end{vmatrix} = 2\xi_r \xi_z, \quad \tilde{\boldsymbol{\xi}}^* \cdot (\hat{\boldsymbol{z}} \times \tilde{\boldsymbol{\xi}}) = \begin{vmatrix} \xi_r & -\xi_\theta & -\xi_z \\ 0 & 0 & 1 \\ \xi_r & \xi_\theta & \xi_z \end{vmatrix} = -2\xi_r \xi_\theta. \quad (3.29)$$

When plugging equations (3.26) and (3.28) into (3.25), it is easy to check that several terms vanish and equation (3.20) is finally obtained. \square

Lemma 3.5. If $k \neq 0$, the squared modulus of ξ can be expressed in terms of ξ_r and ξ_θ through the following relation:

$$|\xi|^2 = \xi_r^2 - \xi_\theta^2 + \frac{1}{k^2} \left(\frac{1}{r} \frac{d(r\xi_r)}{dr} + i \frac{m}{r} \xi_\theta \right)^2 \quad (3.30)$$

Proof. Starting from the incompressibility condition for ξ in cylindrical coordinates, (3.6), the square of the axial component ξ_z can be expressed in terms of ξ_r and ξ_θ , provided $k \neq 0$:

$$\xi_z^2 = -\frac{1}{k^2} \left(\frac{1}{r} \frac{d(r\xi_r)}{dr} + i \frac{m}{r} \xi_\theta \right)^2. \quad (3.31)$$

Thus, using relation (3.8) we get the desired expression for $|\xi|^2$ in terms of ξ_r and ξ_θ only. \square

Comment. Note this expression for ξ_z^2 can be plugged into (3.20) to immediately obtain the generalized energy as a functional of two functions only, as will be seen in Theorem 3.6.

Notation. We will use the dot notation $\dot{\varphi}(r)$ to denote the (radial) derivative of a function φ of one variable. This does not lead to any confusion, since no time variations are being considered.

Theorem 3.6. The generalized energy is given in terms of ξ_r and ξ_θ as an integral functional

$$U(\xi_r, \xi_\theta) = \int_a^b \mathcal{L}(r, \xi_r, \xi_\theta, \dot{\xi}_r) dr. \quad (3.32)$$

where the integrand $\mathcal{L}(r, \xi_r, \xi_\theta, \dot{\xi}_r)$ is given by

$$\mathcal{L} = \frac{\pi L}{\mu_0} \left[r (F^2 + \lambda\rho) \left(\xi_r^2 - \xi_\theta^2 + \frac{1}{k^2} \left(\frac{1}{r} \frac{d(r\xi_r)}{dr} + i \frac{m}{r} \xi_\theta \right)^2 \right) + 4iFB_\theta \xi_r \xi_\theta + \Theta \xi_r^2 \right].$$

3.4 Optimization of the generalized energy

Now that an expression for $U(\xi_r, \xi_\theta)$ has been obtained, we proceed to find its stationary points in order to determine, in virtue of Theorem 2.19, the growth rate of the instabilities for the given configuration. The following result of calculus of variations will be the key tool used in this optimization:

Lemma 3.7. Let $[\xi_i] = (\xi_1, \dots, \xi_n)$ be a tuple of smooth scalar complex functions of one variable r , satisfying given boundary conditions, and consider a smooth real-valued integral functional

$$U[\xi_i] = \int_0^a \mathcal{L}(r, [\xi_i], [\dot{\xi}_i]) dr. \quad (3.33)$$

Then, tuple of paths $[\xi_i]$ that make U stationary is given by the Euler-Lagrange equations:

$$\frac{\partial \mathcal{L}}{\partial \xi_i} - \frac{d}{dr} \left(\frac{\partial \mathcal{L}}{\partial \dot{\xi}_i} \right) = 0. \quad (3.34)$$

Proof. This is a generalization of the well-known Euler-Lagrange theorem result, and its proof can be found in the literature about variations of integral functionals that depend on several one-variable functions. \square

Theorem 3.8. Let (ξ_r^*, ξ_θ^*) be an extreme value of the generalized energy $U(\xi_r, \xi_\theta)$. Then, the component ξ_θ^* is given in terms of ξ_r^* and its radial derivative through

$$\xi_\theta^* = \frac{im}{m^2 + r^2 k^2} \left(r \dot{\xi}_r^* + \xi_r^* + \frac{2k^2 r F B_\theta}{m(F^2 + \lambda\rho)} \xi_r^* \right), \quad (3.35)$$

and ξ_r^* can be found as an extremum of the integral functional

$$U(\xi_r) = \frac{\pi L}{\mu_0} \int_a^b \left(f \dot{\xi}_r^2 + h \dot{\xi}_r \xi_r + g \xi_r^2 \right) dr, \quad (3.36)$$

where the following functions of r have been defined:

$$\begin{aligned} f &= \frac{r^3(F^2 + \lambda\rho)}{m^2 + k^2 r^2}, & h &= \frac{2r^2(F^2 + \lambda\rho) - 4mrFB_\theta}{m^2 + k^2 r^2}, \\ g &= \left(1 + \frac{1}{m^2 + k^2 r^2} \right) r(F^2 + \lambda\rho) - \frac{1}{m^2 + k^2 r^2} \left(4mFB_\theta + \frac{4F^2 B_\theta^2 k^2 r}{F^2 + \lambda\rho} \right) + \Theta. \end{aligned}$$

Proof. A particular case of the previous lemma is that, if \mathcal{L} does not depend on $\dot{\xi}_\theta$, then at an optimum we must have $\partial\mathcal{L}/\partial\xi_\theta = 0$. Thus, starting from expression (3.32), we impose

$$\frac{\partial\mathcal{L}}{\partial\xi_\theta} = \frac{2\pi L r}{\mu_0} \left[(F^2 + \lambda\rho) \left(\frac{im}{r^2 k^2} \frac{d}{dr} (r \xi_r) - \left(1 + \frac{m^2}{r^2 k^2} \right) \xi_\theta \right) + \frac{2iFB_\theta}{r} \xi_r \right] = 0, \quad (3.37)$$

When isolating ξ_θ from the previous expression, expression (3.35) is immediately obtained.

In order complete the optimization of $U(\xi_r, \xi_\theta)$, it is enough to plug this expression into (3.32) as ξ_θ , and optimize the resulting single-input functional $U(\xi_r)$. One is only left to prove this functional is indeed given by (3.36). One way of starting this calculation is by expressing (3.35) as

$$\xi_\theta = \alpha r \dot{\xi}_r + \beta \xi_r, \quad (3.38)$$

where the imaginary dimensional constants A and B (with units of length) are given by

$$\alpha = \frac{im}{m^2 + k^2 r^2}, \quad \beta = \alpha \left(1 + \frac{2k^2 r F B_\theta}{m(F^2 + \lambda\rho)} \right). \quad (3.39)$$

Now, one can immediately obtain that $U(\xi_r)$ has the form (3.36), where

$$\begin{aligned} f &= \frac{r(F^2 + \lambda\rho)}{k^2} [1 + 2im\alpha - (m^2 + k^2 r^2)\alpha^2] \\ h &= 4irFB_\theta\alpha + \frac{2(F^2 + \lambda\rho)}{k^2} [1 + im(\alpha + \beta) - (m^2 + k^2 r^2)\alpha\beta] \\ g &= 4iFB_\theta\beta + \frac{F^2 + \lambda\rho}{k^2 r} [1 + k^2 r^2 + 2im\beta - (m^2 + k^2 r^2)\beta^2] + \Theta \end{aligned}$$

When these expressions are expanded using (3.39), several terms cancel out and the desired result is easily obtained. \square

Notation. Now that the analysis is reduced to just the radial component of ξ , we will use ξ instead of ξ_r for a lighter notation.

Theorem 3.9. The radial component ξ^* of the extrema of U is a solution to the second-order differential equation

$$\frac{d}{dr} \left(f \dot{\xi} \right) - \tilde{g} \xi = 0, \quad (3.40)$$

being f as previously defined, and \tilde{g} given by the expression

$$\begin{aligned} \tilde{g} = & \left(1 - \frac{m^2 - k^2 r^2}{(m^2 + k^2 r^2)^2} \right) r (F^2 + \lambda \rho) \\ & - \frac{k^2 r^2}{m^2 + k^2 r^2} \left[\frac{4mFB_\theta}{m^2 + k^2 r^2} + \frac{\lambda}{k^2} \dot{\rho} + \frac{d|B|^2}{dr} + \frac{2B_\theta^2}{r} \left(\frac{2F^2}{F^2 + \lambda \rho} - 1 \right) \right] \end{aligned} \quad (3.41)$$

Proof. We use the Euler-Lagrange lemma, this time for single-input integral functionals. Thus, letting

$$\mathcal{L}(\xi, \dot{\xi}) = \frac{\pi L}{\mu_0} \left(f \dot{\xi}^2 + h \dot{\xi} \xi + g \xi^2 \right), \quad (3.42)$$

the optimal is given by

$$\frac{\partial \mathcal{L}}{\partial \xi} - \frac{d}{dr} \left(\frac{\partial \mathcal{L}}{\partial \dot{\xi}} \right) = 0. \quad (3.43)$$

We compute the partial derivatives:

$$\begin{aligned} \frac{\partial \mathcal{L}}{\partial \xi} &= \frac{\pi L}{\mu_0} (2g\xi + h\dot{\xi}) \\ \frac{\partial \mathcal{L}}{\partial \dot{\xi}} &= \frac{\pi L}{\mu_0} (2f\dot{\xi} + h\xi) \end{aligned}$$

Thus, the Euler-Lagrange equation is

$$2g\xi + h\dot{\xi} - \frac{d}{dr} (2f\dot{\xi} + h\xi) = 0, \quad (3.44)$$

which can be recast using the product rule into

$$\frac{d}{dr} \left(f \dot{\xi} \right) - \left(g - \frac{1}{2} \dot{h} \right) \xi_r = 0. \quad (3.45)$$

This is of the form (3.40), being $\tilde{g} = g - \dot{h}/2$, so we are left to prove \tilde{g} is indeed given by expression (3.41). This can first be done by using the expression of h , together with

$$\dot{F} = \frac{m}{r^2} (rB_\theta - B_\theta) + kB_z \quad (3.46)$$

to show that:

$$\frac{\dot{h}}{2} = \frac{1}{m^2 + k^2 r^2} \left(\frac{2m^2 r (F^2 + \lambda \rho)}{m^2 + k^2 r^2} + r^2 \lambda \dot{\rho} - \frac{4m^3 F B_\theta}{m^2 + k^2 r^2} + k^2 r^2 \frac{dB_z^2}{dr} + m^2 \Theta \right) \quad (3.47)$$

Then, when subtracting this from g to obtain \tilde{g} , several terms can be simplified to obtain the desired result, (3.41). \square

Comment. Equation (3.40) is our version of equation (14) in Linton et al. (1996), and they can be checked to match for $m = 1$ and $\dot{\rho} = 0$.

3.5 External perturbation solution

The aim of this section is to solve the Euler-Lagrange equation analytically for r in a given interval $I \subset [0, +\infty)$, under the assumption of constant density ($\dot{\rho} = 0$) and no magnetic field ($\mathbf{B} = 0$). Indeed, as justified in Section 3.6, these conditions will later be assumed for the environment of a magnetic flux rope, and will turn out to be useful to study its stability. We start by stating a useful mathematical about a very special type of functions:

Lemma 3.10. The general real solution to the *modified Bessel equation* of order $\nu \in \mathbb{R}$,

$$r^2 \ddot{y} + r\dot{y} - (\nu^2 + k^2 r^2) y = 0, \quad (3.48)$$

is given by

$$y(r) = \alpha K_\nu(|k|r) + \beta I_\nu(|k|r), \quad \alpha, \beta \in \mathbb{R}, \quad (3.49)$$

where I_ν and K_ν are the *modified Bessel functions* of first and second kind, respectively. Some key properties of these functions are:

1. Asymptotic behavior:

$$I_\nu(x) \sim \frac{1}{\sqrt{2\pi x}} e^x, \quad K_\nu(x) \sim \sqrt{\frac{\pi}{2x}} e^{-x}, \quad \text{for } x \rightarrow +\infty. \quad (3.50)$$

2. Derivative recurrence formulas:

$$\dot{I}_\nu(x) = I_{\nu-1}(x) - \frac{\nu}{x} I_\nu(x), \quad \dot{K}_\nu(x) = -K_{\nu-1}(x) - \frac{\nu}{x} K_\nu(x), \quad \text{for } \nu \in \mathbb{R}. \quad (3.51)$$

Proof. These well-known results can be found in any text on ordinary differential equations, such as [Harris \(2014\)](#) or [Zakharov \(2009\)](#). \square

Theorem 3.11. The general solution to the Euler-Lagrange equation (3.40) in conditions of constant density and zero magnetic field is given by

$$\xi(r) = \alpha \dot{K}_m(|k|r) + \beta \dot{I}_m(|k|r), \quad \alpha, \beta \in \mathbb{R}. \quad (3.52)$$

where \dot{K}_m and \dot{I}_m are the first derivatives of the m -th order modified Bessel functions.

Proof. In the conditions stated above, the functions f and \tilde{g} in (3.40) are greatly simplified to:

$$f = \frac{\lambda \rho r^3}{m^2 + k^2 r^2}, \quad \tilde{g} = \left(1 - \frac{m^2 - k^2 r^2}{(m^2 + k^2 r^2)^2}\right) r \lambda \rho. \quad (3.53)$$

Using the product rule for $(f\xi)$ and simplifying some terms, equation (3.40) can be rewritten as a second order linear differential equation:

$$r^2 \ddot{\xi} + \left(1 + \frac{2m^2}{m^2 + k^2 r^2}\right) r \dot{\xi} - \left(m^2 + k^2 r^2 - \frac{m^2 - k^2 r^2}{m^2 + k^2 r^2}\right) \xi = 0. \quad (3.54)$$

In order to find the solutions to this ODE, we will use a *happy idea*, which starts by letting y be a solution of the modified Bessel equation of order m :

$$r^2 \ddot{y} + r\dot{y} - (m^2 + k^2 r^2) y = 0. \quad (3.55)$$

Then, y can be expressed in terms of its derivatives as

$$y = \frac{r}{m^2 + k^2 r^2} (r\dot{y} + \dot{y}). \quad (3.56)$$

On the other hand, (3.55) can be differentiated to obtain

$$r^2 \ddot{y} + 3r\dot{y} + (1 - (m^2 + k^2 r^2)) \dot{y} - 2rk^2 y = 0. \quad (3.57)$$

Plugging (3.56) into (3.57), rearranging terms and letting $\xi = \dot{y}$, we obtain a second order ODE in ξ which coincides with (3.54). However, we know that two linearly independent solutions to (3.55) are the modified bessel functions: $y = I_m(|k|r)$ and $y = K_m(|k|r)$. This gives us the general solution to the second-order ODE (3.54):

$$\xi(r) = \alpha \dot{K}_m(|k|r) + \beta \dot{I}_m(|k|r), \quad (3.58)$$

for some $\alpha, \beta \in \mathbb{R}$. \square

3.6 Free-boundary conditions: assumptions

In this section, we present some additional assumptions that are used in Linton et al. (1996) before imposing the free-boundary conditions to determine the growth rate of the configuration. While we will follow them too, we present them here and compare them to some real data gathered from space missions. The following plots have been extracted from Masiás-Meza et al. (2016), and display the result of processing and averaging data regarding more than 40 coronal mass ejection events.

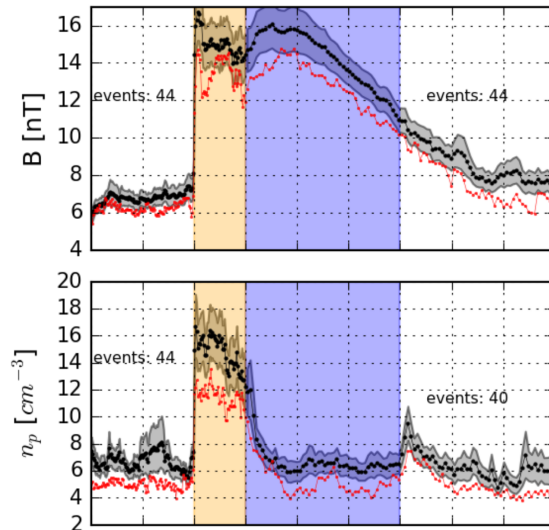


Figure 3.4: The top plot shows the magnetic field modulus, and the bottom shows the proton density, both as a function of time (expressed in units normalized to the event duration). The *sheath* of the CMEs is shaded with an orange background, and the blue background corresponds to the MFR structure. Extracted from Masiás-Meza et al. (2016).

The first key assumption consists in stating that, beyond the distance $r = R$, the plasma volume merges with the embedding solar wind, which has a magnetic field $\mathbf{B}_{\text{wind}} = 0$ for $r > R$. This is not a perfect assumption: observations show the magnetic field in the solar wind usually around $|\mathbf{B}_{\text{wind}}| \approx 5 \text{ nT}$ ¹, while the magnetic field inside the MFR is found in the range of 10 nT to 15 nT , as seen in Figure 3.4, and can be even larger when closer to the Sun. Although these quantities are comparable to the field in the solar wind, they are several times larger, making this assumption somehow reasonable. Furthermore, it is also convenient, since a vanishing external field has cylindrical symmetry, so the Euler-Lagrange equation (3.40) can be also be applied to that region.

¹This value changes a lot overtime, depending on the solar cycle.

Another key assumption in Linton et al. (1996) is that the magnetic field \mathbf{B} discontinuously drops to zero at $r = R$. Of course, this is just an approximation of reality, but observations shown in 3.4 closely match the idea that B drastically decreases near the boundary of the magnetic flux rope. This is particularly true in the sheath of the CME, while in the tail it's just a continuous but quite steep transition towards the field in the solar wind.

Finally, the last assumption consists in considering a constant density, $\rho(r) = \rho_0$, for all $r > 0$. This can be justified using the following plot in Figure 3.4 for the proton density (number of protons per unit volume), which except in the case of the sheath, the density in the MFR matches quite well the one in the solar wind. Note that, using a value of $n_p = 5$ particles per cm^3 , we can use equation (1.13) to estimate the fluid density in the flux rope as:

$$\rho_0 \approx 1.16 \rho_p = 1.16 m_p n_p \approx 9.7 \cdot 10^{-24} \text{g/cm}^3. \quad (3.59)$$

3.7 Free-boundary conditions: equations

Now, we are in conditions of obtaining boundary condition equations from Linton et al. (1996), but generalized for instabilities of any order m . As can be seen in the assumptions previously explained, no particular boundary condition is being assigned to ξ : indeed, the true boundary condition is set at infinity, and is requiring that the perturbation is localized:

$$\lim_{r \rightarrow \infty} \xi(r) = 0. \quad (3.60)$$

Indeed, this can be seen as a consequence of the displacements having compact support, as developed theoretically in Chapter 2. Moreover, the perturbation displacement as a function $\xi : \mathbb{R}^3 \rightarrow \mathbb{R}^3$ is required to be smooth, with the exception of the MFR boundary, where a discontinuity in the magnetic field is accounted for with a discontinuity in $\dot{\xi}$ ².

Lemma 3.12. Let f be a piece-wise smooth function with only one discontinuity at $r = R$. For simplicity, we use the following notation for the lateral limits:

$$f(R) = \lim_{\varepsilon \rightarrow 0^+} f(R - \varepsilon), \quad f_{\text{wind}} = \lim_{\varepsilon \rightarrow 0^+} f(R + \varepsilon) \quad (3.61)$$

Let g be a continuous function. Then, the following equality holds:

$$\lim_{\varepsilon \rightarrow 0^+} \int_{R-\varepsilon}^{R+\varepsilon} g(r) \dot{f}(r) dr = g(R) (f_{\text{wind}} - f(R)). \quad (3.62)$$

Proof. Using the continuity of f for $r \neq R$, it is immediate the approximation

$$f(r) \approx (f_{\text{wind}} - f(R)) \chi(r - R) + f(R) \quad (3.63)$$

for $r \in (R - \varepsilon, R + \varepsilon)$ becomes arbitrarily accurate when $\varepsilon \rightarrow 0$, so

$$\lim_{\varepsilon \rightarrow 0^+} \int_{R-\varepsilon}^{R+\varepsilon} g(r) \dot{f}(r) dr = \lim_{\varepsilon \rightarrow 0^+} \int_{R-\varepsilon}^{R+\varepsilon} g(r) [(f_{\text{wind}} - f(R)) \dot{\chi}(r - R) + f(R)] dr. \quad (3.64)$$

Now, using the following property for the Dirac delta $\delta = \dot{\chi}$,

$$\int_{R-\varepsilon}^{R+\varepsilon} g(r) \delta(r) dr = g(R) \quad \text{for all } \varepsilon > 0, \quad (3.65)$$

²Although in Chapter 2 the theory assumes the displacements are smooth over \mathbb{R}^3 , a similar reasoning could be used to prove the same results imposing smoothness for ξ in $\mathbb{R}^3 \setminus \partial V$, the open set of \mathbb{R}^3 that excludes the boundary of the magnetic flux rope.

the desired result is immediately obtained. \square

Lemma 3.13. Following the notation introduced in (3.61), the boundary condition for ξ at the magnetic flux rope boundary $r = R$ is given by

$$k^2 |\mathbf{B}(R)|^2 \xi(R) + (F^2(R) + \lambda\rho) R \dot{\xi}(R) - \lambda\rho R \dot{\xi}_{\text{wind}} = 0. \quad (3.66)$$

Proof. Applying the previous section's separately for $r < R$ and $r > R$, we find the Euler-Lagrange equation (3.40) must hold independently for $r < R$ and $r > R$. The point $r = R$ has measure zero, so for any small $\varepsilon > 0$:

$$\int_{R-\varepsilon}^{R+\varepsilon} \left[\frac{d}{dr} (f \dot{\xi}) - \tilde{g} \xi \right] dr = 0, \quad (3.67)$$

and in particular,

$$\lim_{\varepsilon \rightarrow 0^+} \int_{R-\varepsilon}^{R+\varepsilon} \left[\frac{d}{dr} (f \dot{\xi}) \right] dr - \lim_{\varepsilon \rightarrow 0^+} \int_{R-\varepsilon}^{R+\varepsilon} \tilde{g} \xi dr = 0. \quad (3.68)$$

We proceed to compute both limits separately. The first one can be found using the fundamental theorem of calculus:

$$\lim_{\varepsilon \rightarrow 0^+} \int_{R-\varepsilon}^{R+\varepsilon} \left[\frac{d}{dr} (f \dot{\xi}) \right] dr = \lim_{\varepsilon \rightarrow 0^+} [f \dot{\xi}]_{R-\varepsilon}^{R+\varepsilon} = \frac{R^3}{m^2 + k^2 R^2} [\lambda\rho \dot{\xi}_{\text{wind}} - (F^2(R) + \lambda\rho) \dot{\xi}(R)] \quad (3.69)$$

On the other hand, using the previous lemma:

$$\lim_{\varepsilon \rightarrow 0^+} \int_{R-\varepsilon}^{R+\varepsilon} \tilde{g} \xi dr = \lim_{\varepsilon \rightarrow 0^+} \int_{R-\varepsilon}^{R+\varepsilon} \left(\frac{-k^2 r^2}{m^2 + k^2 r^2} \xi \right) \frac{d|\mathbf{B}|^2}{dr} dr = \frac{k^2 R^2 |\mathbf{B}(R)|^2}{m^2 + k^2 R^2} \xi(R). \quad (3.70)$$

The proof is completed by plugging these expressions into (3.68) and rearranging the terms. \square

Theorem 3.14. The boundary condition at $r = R$ for the Euler-Lagrange equation (3.40) is given by

$$\left[k^2 |\mathbf{B}(R)|^2 - \lambda\rho |k| R \frac{\ddot{K}_m(|k|R)}{\dot{K}_m(|k|R)} \right] \xi(R) + (F^2(R) + \lambda\rho) R \dot{\xi}(R) = 0, \quad (3.71)$$

which can also be expressed in terms of modified Bessel functions as

$$\left[k^2 |\mathbf{B}(R)|^2 + \lambda\rho \left(1 + \frac{(m^2 + k^2 R^2) K_m(|k|R)}{|k|R K_{m-1}(|k|R) + m K_m(|k|R)} \right) \right] \xi(R) + (F^2(R) + \lambda\rho) R \dot{\xi}(R) = 0.$$

Proof. Firstly, we want to find an expression for $\dot{\xi}_{\text{wind}}$ in terms of the internal values of ξ . Note that, using result (3.52), the perturbation can be solved for $r > R$: there must exist an $\alpha \in \mathbb{R}$ such that

$$\xi(r) = \alpha \dot{K}_m(|k|r) \quad (3.72)$$

Indeed, this must be the case for the perturbation to be localized, since property (3.50) shows that \dot{K}_m vanishes when $r \rightarrow \infty$, while \dot{I}_m diverges. This expression can be differentiated to obtain

$$\dot{\xi}(r) = \alpha |k| \ddot{K}_m(|k|r), \quad (3.73)$$

and continuity of ξ at $r = R$ yields

$$\dot{\xi}_{\text{wind}} = \alpha |k| \dot{K}_m(|k|R) = |k| \frac{\ddot{K}_m(|k|R)}{\dot{K}_m(|k|R)} \xi(R). \quad (3.74)$$

The boundary condition (3.71) is now immediately obtained by plugging this expression into (3.66). The second expression can be obtained using the modified Bessel equation (3.48) for $y = K_m(|k|r)$ and evaluating it at $r = R$:

$$\frac{\ddot{K}_m(|k|R)}{\dot{K}_m(|k|R)} = -\frac{1}{|k|R} \left(1 - \frac{(m^2 + k^2 r^2) K_m(|k|R)}{|k|R \dot{K}_m(|k|R)} \right). \quad (3.75)$$

Now, using the derivative recurrence formula (3.51) for \dot{K}_m , yields

$$-|k|R \frac{\ddot{K}_m(|k|R)}{\dot{K}_m(|k|R)} = 1 + \frac{(m^2 + k^2 r^2) K_m(|k|R)}{|k|R K_{m-1}(|k|R) + m K_m(|k|R)}, \quad (3.76)$$

as we wanted to prove. \square

Comment. It should be observed that, as expected, this method is invariant to a change in sign of the wave numbers. Indeed, if we change (m, k) to $(-m, -k)$, both the Euler-Lagrange equation (3.40) and the boundary condition (3.66) remain unaltered. Hence, as was explained commented in Section 3.2, the analysis can restricted to the perturbations with non-negative azimuthal wave numbers, $m \geq 0$.

4 . Application of the method

4.1 Magnetic flux rope modeling

The stability analysis that has been developed in the previous chapters starts by fixing a given equilibrium magnetic field configuration $\mathbf{B}(\mathbf{r})$. In this section we describe the internal magnetic structures that are commonly found in CMEs, while presenting some models that will be fundamental to our study of flux rope stability via the application of the growth rate method.

As mentioned in Chapter 1, measurements of the heliospheric magnetic fields are constantly made *in situ* via the magnetometers equipped in spacecrafts currently orbiting the Sun. This is the case, for instance, of Solar Orbiter's MAG instrument, or Parker Solar Probe's FIELDS. When a CME takes place and propagates through the Solar System, the instruments that find themselves in the way measure the magnetic field along their path one-dimensional, which can then be used to infer the whole structure of the flux rope. A common way to do so is by using the Grad-Shafranov reconstruction method, which starts by assuming an ideal MHD equilibrium configuration (2.9), and then solves numerically a PDE to obtain the magnetic potential, and hence the magnetic field, throughout the whole flux rope cross-section (Hu and Sonnerup (2001), Möstl et al. (2009)).

The patterns observed in the reconstructed magnetic field data are then used by scientists to develop models describing the internal magnetic configuration of MFRs at equilibrium. Such models give the axial and azimuthal components of the field in terms of certain parameters, which can be tweaked to account for the diversity of possible flux rope profiles. The models we will work with assume cylindrical symmetry, as introduced in Section 3.1, and give the magnetic field in terms of the normalized distance to the axis $\bar{r} = r/R$, being R the radius of the flux rope¹. Another very common parameter is the amplitude of the magnetic field B_0 , which coincides with the maximum axial field and provides the model with dimensions, serving as a scale factor.

One of the key models recently used for MFR fittings is the Circular-Cylindrical (CC) model introduced in Nieves-Chinchilla et al. (2016), which has served as a basis for many publications, including recent papers which have generalized it to describe geometries with distorted cross-sections and arbitrarily curved axis (Nieves-Chinchilla et al. (2018), Weiss et al. (2022)). After fixing integers² $n \geq 1$ and $m \geq 0$, the CC model has two parameters $C_{nm}, \tau > 0$ which determine the magnetic field. Its axial component has a maximum value of B_0 at the axis and decreases from there, while the azimuthal is zero at the axis and increases with the distance from it.

$$B_z(\bar{r}) = B_0 \left(1 - \frac{1}{\tau} \bar{r}^{n+1} \right), \quad B_\theta(\bar{r}) = \frac{B_0}{\tau C_{nm}} \bar{r}^{m+1}. \quad (4.1)$$

This model is particularly relevant to this work since the recent Florido-Llinas et al. (2020) uses the growth rate method to study the combinations of parameters (C_{nm}, τ) that lead to an equilibrium magnetic field that are kink unstable. The results are summarized in the following plot in Figure 4.1: it shows that configurations given by small values of C_{nm} and τ are kink unstable, while higher values of the parameters yield kink stable configurations.

¹During observations, the radius R is fitted along with the rest of the model parameters.

²The values $n = 1$ and $m = 0$ are the most used within flux rope fittings.

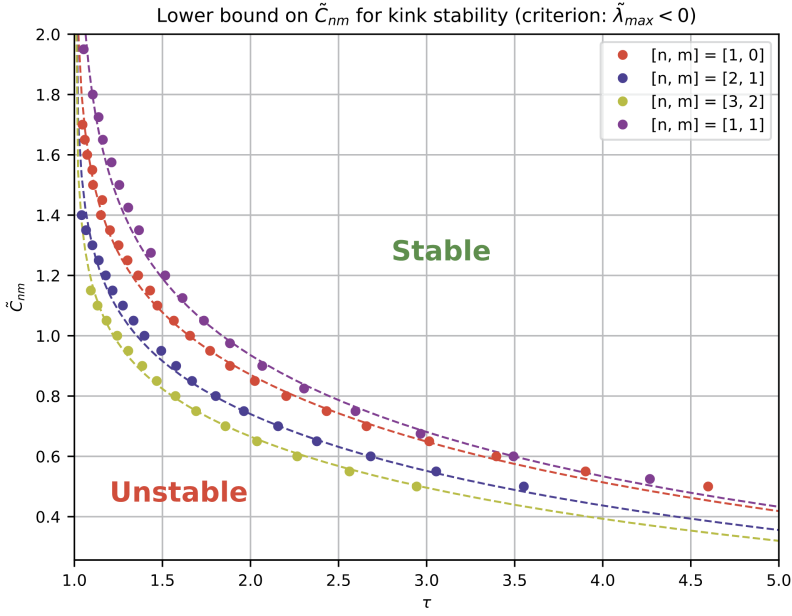


Figure 4.1: Kink stability analysis of the CC Nieves-Chinchilla model, from [Florido-Llinas et al. \(2020\)](#).

The unstable configurations in the plot can be checked to correlate very well with the ones that exhibit the highest degree of twist around the axis. This is in agreement with [Knizhnik et al. \(2018\)](#), which explains how the kink instability tends to occur in flux ropes that are highly twisted. The configurations which were found to be unstable, however, also coincide with the ones having higher Lorentz forces $\mathbf{J} \times \mathbf{B}$ inside the flux rope. In fact, [Florido-Llinas et al. \(2020\)](#) suggests the presence of Lorentz forces, particularly if they are present in different directions and there are inward forces near the edge, could be related to the occurrence of such instabilities.

4.2 The Gold-Hoyle modified model

In order to further explore the conclusions in [Florido-Llinas et al. \(2020\)](#) and identify the key drivers behind the kink instability, as well as behind the instabilities of other azimuthal wave numbers m , we require a model which can lead to both highly twisted and force-rich magnetic field configurations, but not necessarily for the same combinations of parameters. Then, we will be able to perform a similar analysis to the one in Figure 4.1 to characterize the stability of each configuration and, therefore, identify the MFR properties that may be triggering the development of plasma instabilities. We start by giving a brief introduction to the twist and Lorentz forces in a MFR with cylindrical geometry, in a view to introduce the model that we have developed.

The *twist* of a MFR is defined as the angle around the axis covered by the magnetic field lines, measured per unit length. The twist is noted by Q , and it is a function of the distance to the axis due to the radial dependence of the magnetic field. Basic geometrical considerations lead to the following expression³ of the twist:

$$Q(r) = \frac{B_\varphi(r)}{r B_z(r)}. \quad (4.2)$$

On the other hand, the Lorentz forces in the flux rope, as previously explained, are given by the cross product of the current density $\mathbf{J} \times \mathbf{B}$, with $\mathbf{J} = \nabla \times \mathbf{B}/\mu_0$ due to Ampere's law (1.4). In a cylindrical MFR, the Lorentz force can be expressed in terms of just the distance to the axis, and

³See [Florido-Llinas \(2020\)](#) for a detailed explanation.

an automatic calculation shows it has only a radial component:

$$\mathbf{J} \times \mathbf{B} = - \left(\frac{1}{2} \frac{dB_z^2}{dr} + \frac{B_\theta}{r} \frac{d}{dr} (rB_\theta) \right) \hat{\mathbf{r}}. \quad (4.3)$$

Hence, an evaluation of the sign of its radial gives information about whether it is directed outwards (positive) or inwards (negative).

Now we are in conditions of defining the cylindrical magnetic field model that will be used in this work. Other than the field amplitude B_0 , the cylindrical magnetic field model we now introduce has two adimensional parameters: q and α . For $\alpha = 1$ we recover the Gold-Hoyle model, first presented in [Gold and Hoyle \(1960\)](#), which is well known for giving a uniformly-twisted⁴ force-free magnetic field. The field components in the *Gold-Hoyle modified model* are defined as

$$B_z(\bar{r}) = \frac{B_0}{1 + q^2\bar{r}^2}, \quad B_\theta(\bar{r}) = q\bar{r}^\alpha B_z(\bar{r}). \quad (4.4)$$

The following plot shows a comparison between both models field models, for parameter combinations which yield similar structures: Let's take a closer look into the physical interpretation of the

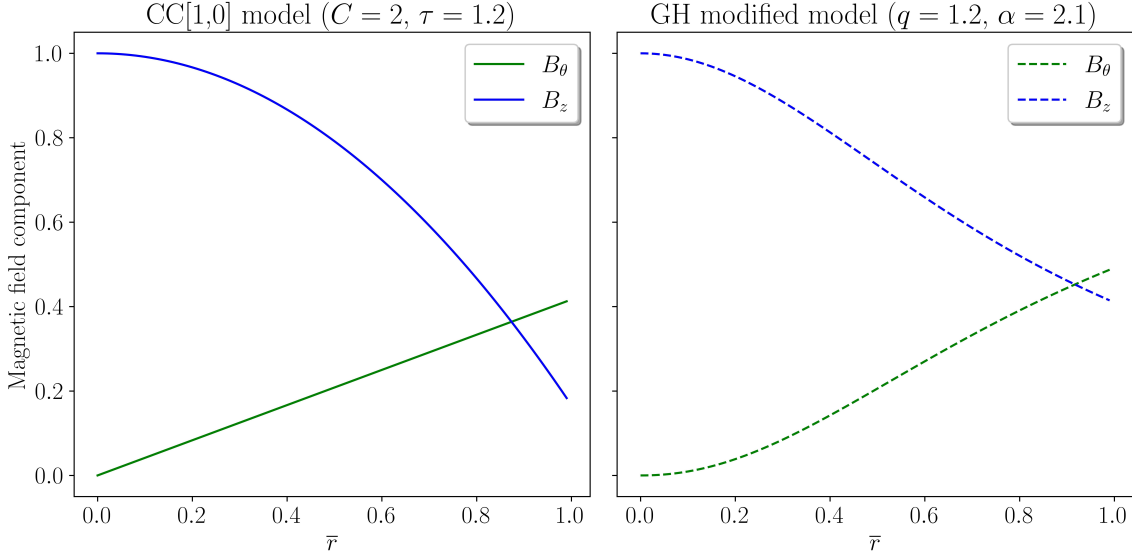


Figure 4.2: Comparison between the CC model from [Nieves-Chinchilla et al. \(2016\)](#) and the Gold-Hoyle modified model introduced in this work.

parameters we have introduced in (4.4). We call q the *twist parameter*. Indeed, using expression (4.2), we see the Gold-Hoyle model ($\alpha = 1$) has constant twist is $Q = q/R$, so q is an adimensional interpretation of the twist. Furthermore, if $\alpha \neq 1$, q is still directly proportional to the twist at any axial distance:

$$Q(\bar{r}) = q\bar{r}^{\alpha-1}/R. \quad (4.5)$$

Furthermore, we call α the *force parameter*, since its change from $\alpha = 1$ leads to the presence of forces in the structure. Indeed, letting $\alpha = 1$ and starting from (4.4), the radial current density distribution is found to be

$$\mu_0 \mathbf{J}(r) = \nabla \times \mathbf{B}(r) = \frac{2q}{1 + q^2r^2} \mathbf{B}(r), \quad (4.6)$$

so using Ampere's law we obtain \mathbf{J} is parallel to \mathbf{B} , and the Lorentz forces vanish: $\mathbf{J} \times \mathbf{B} = 0$. Hence, for $\alpha = 1$, the structure is force-free. However, if we start to increase α , magnetic forces come into play. A quick analysis shows that increasing the value of α by fixing q always leads to an increase in the Lorentz forces, which are mostly directed outwards except for the region near the

⁴That is, the twist $Q(r)$ is a constant function.

edge, where they are pointed towards the interior, which Florido-Llinas et al. (2020) pointed out as a potential indicator of kink unstable structures. Moreover, increasing the value of α decreases the twist in the structure. These properties, which are shown in Figure 4.3, make the Gold-Hoyle modified model an appropriate tool to conduct our analysis.

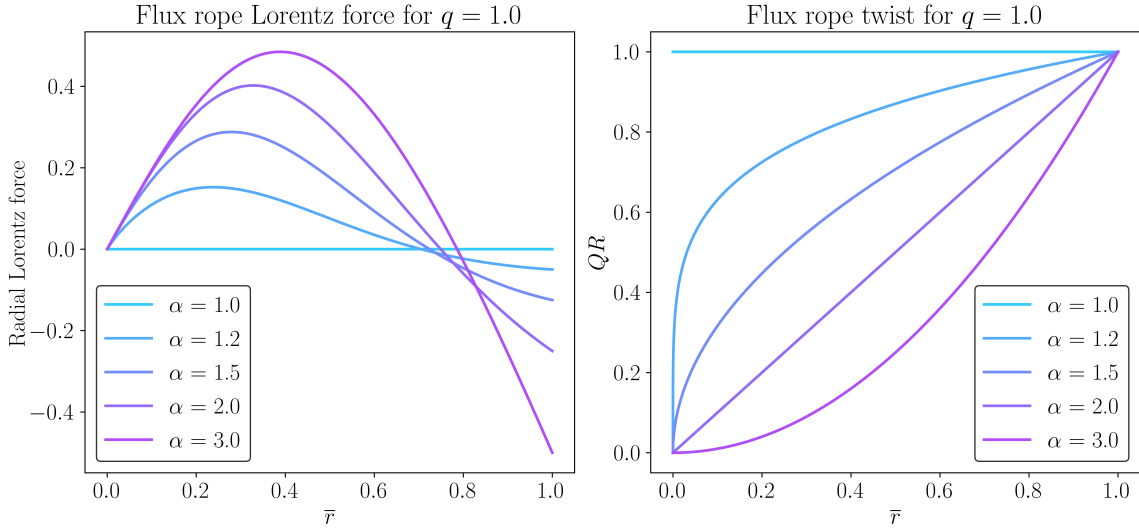


Figure 4.3: MFR Lorentz forces (with $\mu_0 = 1$) and twist for the Gold-Hoyle modified model.

Note that the sign of q only changes the flux rope chirality, so we can restrict the analysis to $q > 0$ without loss of generality. Moreover, we consider only $\alpha \geq 1$ since having $\alpha < 1$ would imply through (4.5) an unbounded twist near the axis, which contradicts MFR observations.

4.3 Implementation of the growth rate method

In this section we apply the method developed in Chapter 3 to characterize the instabilities of the cylindrical magnetic flux rope configurations given by the Gold-Hoyle modified model. The stability analysis starts by recalling equation (3.71), which is of the form

$$D(\lambda; k) = 0 \quad (4.7)$$

for a given function $D : \mathbb{R} \rightarrow \mathbb{R}$, the *dispersion function*, which has λ as a variable, and takes the axial number $k \in \mathbb{R}$ as a parameter. This function also requires other inputs, starting with the equilibrium magnetic field components B_θ and B_z , which are parametrized via α and q via the expressions of the model, (4.4). The value of the azimuthal wave number $m \in \mathbb{Z}$, determining the type of instability, is also a given parameter. Furthermore, we set $B_0 = 1$, $\rho = 1$ and $R = 1$ to simplify the analysis: the results can therefore be thought of as being expressed in a new system of units, which is perfectly valid to obtain qualitative conclusions and identify instability patterns.

Given the value of λ , before evaluating $D(\lambda; k)$ one needs to determine the value of $\xi(R)$ and $\dot{\xi}(R)$ by solving the Euler-Lagrange equation (3.40), which gives the radial component⁵ of the minimal mode⁶. Before solving the ODE, boundary conditions for ξ and $\dot{\xi}$ must be set. Similarly to the analyses carried out by Linton et al. (1996) and Florido-Llinas et al. (2020), we impose the following boundary conditions at the axis:

$$\begin{cases} \xi(0) = 1, \\ \dot{\xi}(0) = 0. \end{cases} \quad (4.8)$$

⁵Although this is the only component that will be required for this analysis, the others can be obtained through relations (3.31) and (3.35).

⁶This mode is not minimal in the same strict sense as introduced in Chapter 2, since we are assuming certain values of m and k which limit the set of displacement perturbations being considered to the ones given by (3.4).

Indeed, the second condition is necessary to satisfy the smoothness of the displacement at the axis. Furthermore, the solutions to the Euler-Lagrange equation (3.40) are determined up to a scale factor, since it is linear and homogeneous, so the solution will be scaled by the value of $\xi(0)$. Hence, setting $\xi(0) = 1$ is enough since finding the zeros of the dispersion function only requires to find the value of $\dot{\xi}(R)/\xi(R)$, which is independent of any scale factor in the solution. The numerical resolution of this initial value problem, as well as the codes used for this analysis, have been developed in Python and can be found in this [Github](#) repository⁷.

Following the procedure indicated above, the dispersion function can be evaluated for any $\lambda \in \mathbb{R}$, and its zeros can be found. If there exists a $\lambda > 0$ such that $D(\lambda; k) = 0$. Then, the structure is unstable to displacements of axial wave number k , with growth rate $\sigma = \sqrt{\lambda}$, which are automatically obtained by finding the zero of the dispersion equation. If more than one zero is found, the highest one is chosen: indeed, as shown in Theorem 2.15, σ should be an upper bound for the exponential growth of the instabilities in a given configuration. Then, the *dispersion relation* can be defined to be the one-to-one function assigning $\lambda = \sigma^2$ to each unstable k :

$$\lambda(k) = D^{-1}(0; k). \quad (4.9)$$

For convenience, will work with λ instead of σ and often refer to it as the growth rate.

4.4 Determining of the dispersion relation

The implementation of this method has given different results depending on the type of instability. For $m = 0$, no zeros of the dispersion function have been found for any value of k , suggesting that the sausage instability does not take place for cylindrical plasmas with the magnetic structure we are considering. We have also been able to check that, for displacements with $m < 0$, the stability results are identical to the ones obtained for $m > 0$, except for a change in the sign of k , as expected. Therefore, the following analysis only focuses in instabilities with $m \geq 1$.

One of the first really interesting results has been that the wave numbers k leading to the most rapidly growing instabilities have been found to be related with the twist parameter of the magnetic field through:

$$k \approx -mq. \quad (4.10)$$

This can be observed in the following plots of the dispersion function for $m = 1$ and $m = 2$:

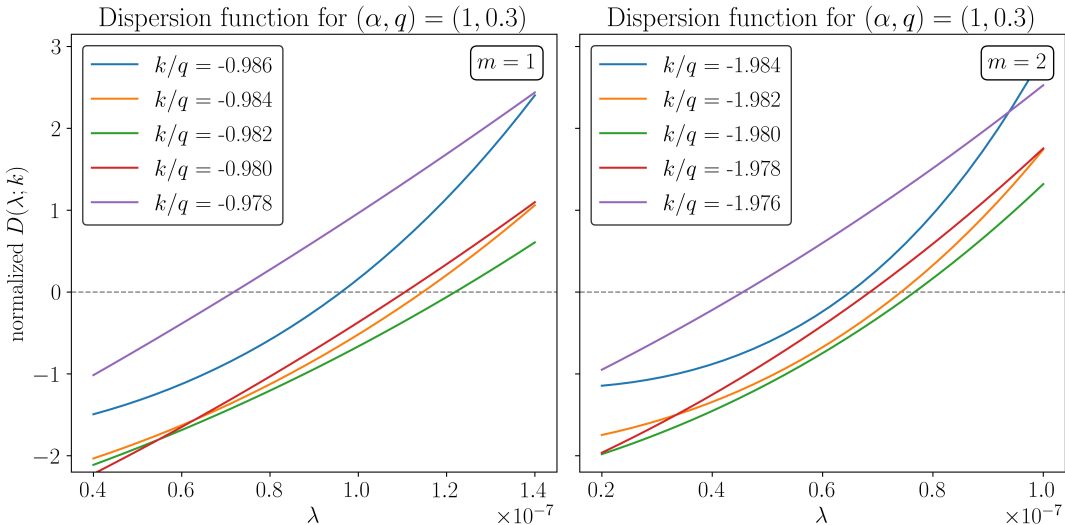


Figure 4.4: Dispersion function for $m = 1$ (left) and $m = 2$ (right), and several values of $k \approx -mq$.

⁷The Python functions used to solve the Euler-Lagrange equation have been adapted from the codes developed in [Florido-Llinas et al. \(2020\)](#) to study the kink instability.

As can be seen in Figure 4.4, for the arbitrary parameters ($\alpha = 1, q = 0.3$), when k is increased starting at $-mq$, the zero of the dispersion increases, reaches a maximum (which corresponds to the green curve in both plots), and then decreases again, rapidly tending to zero. Furthermore, the values of k for which instabilities are being found can be validated with the literature: as explained in Linton et al. (1996), the studies (including theirs) on the kink instabilities of Gold-Hoyle configurations have found instabilities in the near neighborhood of $k > -q$. This coincides is found in agreement with our results. Moreover, for each value of k , the dispersion function grows without bound for large values of λ , so the dispersion function does not have any greater roots than the ones shown in Figure 4.4.

Furthermore, as explained in equation (4.9), the dispersion equation can be solved for λ by finding the root of the dispersion function, leading to the dispersion relation $\lambda(k)$. The results are shown below, and they are compared for different values of the twist parameter q :

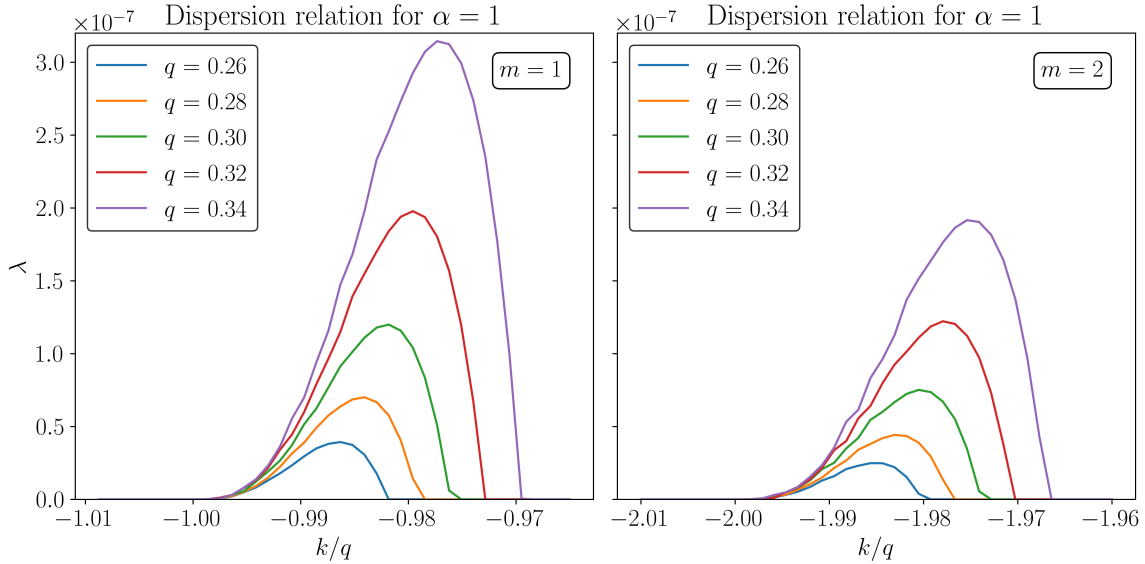


Figure 4.5: Dispersion relation for the Gold-Hoyle model, compared for $m = 1, 2$ and for different values of the twist q .

The first relevant conclusion that stands out from the plots in Figure 4.5 is that there is a quite small range of values of k , quite close to $-mq$, which lead to instabilities: outside of such range, the growth rate rapidly drops to zero, becoming insignificant when compared with the maximum growth rate that can be attained. Moreover, when comparing the plots to each other, we see that the growth rates are larger for $m = 1$ than $m = 2$, implying that, in a force-free Gold-Hoyle configuration ($\alpha = 1$), the kink instability develops way faster than the elliptical instability.

4.5 Obtaining the maximum growth rate

We also observe in each of the plots in Figure 4.5 how an increase in the twist parameter q leads to a uniform increase of the growth rates, as well as a wider range of wave numbers k leading to an instability. This is in agreement with the literature, as pointed out in Section 4.1: highly twisted structures should be the more kink unstable. This same statement also seems to transfer well to instabilities of higher order m , as can be seen in the $m = 2$ plot.

However, it is difficult to study the relationship between growth rate and q with so many variables to account for. Since all the dispersion relation curves seem to have similar shapes, its information can be condensed into just one quantity, for which we will choose their maximum value. We therefore proceed to define a new metric, the maximum growth rate, which allows us to eliminate the k parameter and assign a single growth rate to every magnetic field configuration (α, q) , provided the order m of the instability:

$$\lambda_{\max} = \max_{k \in \mathbb{R}} \lambda(k) = \max_{k \in \mathbb{R}} D^{-1}(0; k). \quad (4.11)$$

This magnitude will also be referred to as the growth rate of the configuration. We now show the results of determining the maximum growth rate when changing the twist parameter q , comparing the results in the same plot for instabilities of different order m . On top of that, we display the first stability results for a structure which is not force-free, increasing the force parameter to $\alpha = 1.5$.

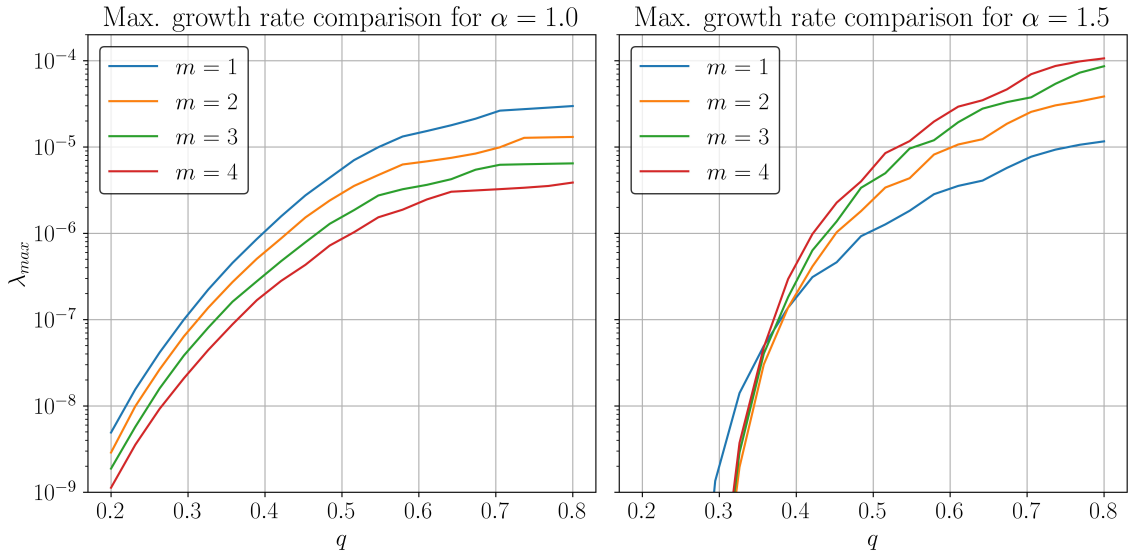


Figure 4.6: Maximum growth rate for magnetic field configurations with $\alpha = 1.0$ (force-free) and $\alpha = 1.5$ (with Lorentz forces), and increasing twist parameter. The results are compared for instabilities of different order, m .

In these plots we see in a more clear way how increasing the twist of a MFR leads to an increase in the growth rate of its instabilities of any order m . The plot in the left, representing force-free Gold-Hoyle structures, shows a clear dominance of the kink instability with respect to other instabilities for any flux rope twist: when m increases, the growth rates become smaller, as was already expected from the results obtained in Figure 4.5 for $m = 1$ and $m = 2$.

Nevertheless, the plot on the right, which illustrates a structure in the presence of Lorentz forces, shows that when the twist parameter is high enough the dominance of the kink instability no longer holds, and higher order instabilities evolve faster in time. This result is particularly relevant, since it provides a counter-example to the generalization of the comparison theorem proven in Newcomb (1960) (explained in Section 3.2) to the modern notion of σ -stability which was later introduced in Goedbloed (1974). Indeed, we see that our magnetic field configurations for $\alpha = 1.5$ and $q \geq 0.4$ are more σ -stable to kink perturbations than to displacements of higher order m . However, this only happens if q is high enough: for small values of the twist parameter, the kink instability remains dominant.

Notice that the vertical axis in Figure 4.5 has a logarithmic scale due to the very rapid increase of the growth rate for small values of q . However, when the flux rope gets more and more twisted, the growth rate does not increase as fast and seems to reach a roughly stationary value. The fact that such a relation is increasing means we can define a unique value of q at which a given threshold growth rate λ_0 is reached. Such a threshold, which should be chosen appropriately depending on the time scale of the system under study, can be used to define a σ -stability: any configuration with a growth rate higher than λ_0 is unstable, while smaller growth rates are regarded as stable despite of the time evolution being exponential. Using this procedure, stability plots like the one shown in Figure 4.1 for the kink instabilities the Nieves-Chinchilla et al. (2016) CC model can be obtained for instabilities of any order m in the Gold-Hoyle modified magnetic field configurations.

4.6 Stability plots

The critical q at which the growth rate λ_{\max} coincides with the threshold λ_0 can be found efficiently using a dichotomic search algorithm and the intermediate value theorem, using the increasing behavior of the function $\lambda_{\max}(q; \alpha)$ shown in Figure 4.6 for different values of α and m . In order for the procedure to work, a suitable initial interval containing the critical value of q is required, as well as a tolerance which dictates to which degree of precision to which q shall be determined. This method determines a stability curve $q(\alpha)$, which separates stable configurations (below the curve) from unstable ones (found above). Some of the results we have obtained are presented below:

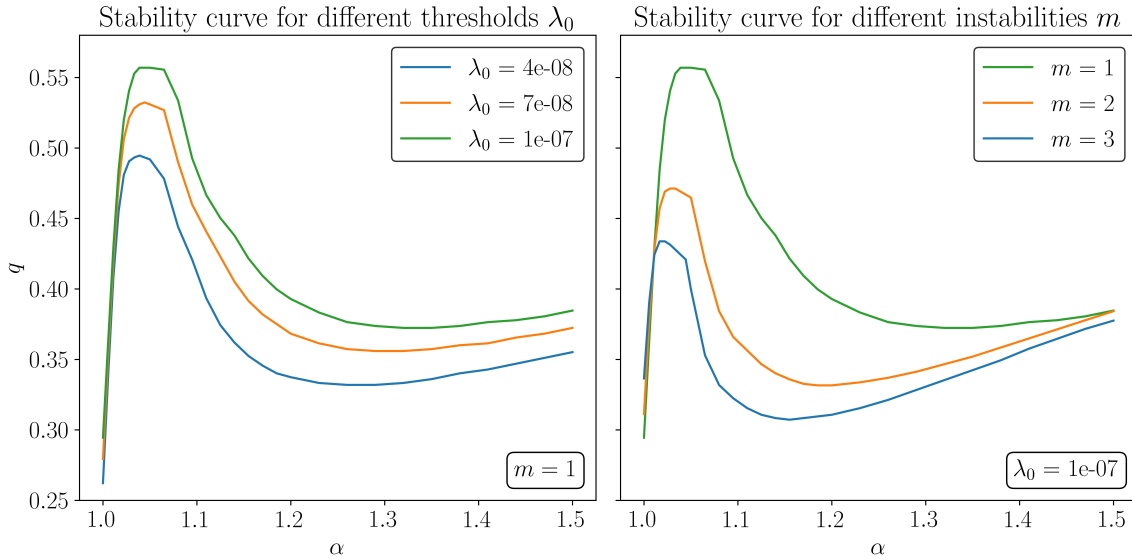


Figure 4.7: Stability curves for different stability thresholds (left) and different types of instability (right). The pairs (α, q) lying above a stability curve are considered stable, while the ones below are unstable.

The plot on the left shows the kink stability curves for different arbitrary thresholds. Starting at $\alpha = 1$ with the force-free configurations, a small increase of the force parameter leads to a very sudden increase in the value of the critical q , which means that such configurations are way more stable than the force-free ones. The maximum stability is reached for $\alpha \approx 1.05$, and a further increase in the forces in the structure leads to a lower stability. For $\alpha > 1.3$, the curve steadily increases, but this time the growing behavior continues quite linearly for way larger values of α . Because of this reason, we name the phenomenon taking place for $\alpha \approx 1.05$ as *superstability*. Although the range of values of α that are relevant to MFR fittings are of the order of $\alpha \in [1, 5]$, we have decided to show the stability curves in the range $\alpha \in [1, 1.5]$ to illustrate the superstability that takes place with more precision.

A first result obtained from this first plot is that the most kink unstable configurations for the Gold-Hoyle modified model, fixing the parameter q , are the ones that are force-free ($\alpha = 1$). In general, fixing q while increasing α , which leads to an increase in the Lorentz forces while decreasing the twist, has a stabilizing effect. This happens even though such forces, as shown in Figure 4.3, are found in opposite directions and directed inwards near the edge of flux rope. This suggests that the instabilities found in [Florido-Llinas et al. \(2020\)](#) for the CC model are in fact more related to the high twist of such configurations than to the internal Lorentz forces in the flux rope structure.

Now, let's examine the plot to the right of Figure 4.7, comparing different types of instability for the same threshold λ_0 . Although for $\alpha = 1$ the kink instability dominates with the largest growth rate, as seen in Figure 4.6, a very small increase in the force parameter rapidly makes the kink perturbations the most stable of all. Hence, we see a dominance of the cross-section instabilities $m = 2$ and $m = 3$ for almost all the configurations being represented except for the force-free ones. This suggests that Lorentz forces tend to enhance the growth rates of higher order instabilities with respect to the kink instability, affecting the geometrical evolution of instabilities.

A perhaps more illustrative way to understand the previous plots is to compare the stability curves with the actual values of the twist and Lorentz forces within the MFR. These magnitudes depend on the distance to the axis, so a reasonable way to quantify them numerically is by averaging their absolute value over the cross section of the flux rope. This can be done through simple integration:

$$\langle f(\alpha, q) \rangle = \frac{1}{S} \int f dS = \frac{1}{\pi} \int_0^{2\pi} d\theta \int_0^1 \bar{r} f(\bar{r}; \alpha, q) d\bar{r} = 2 \int_0^1 \bar{r} f(\bar{r}; \alpha, q) d\bar{r}, \quad (4.12)$$

where $f(r)$ can be the twist $Q(r)$ or the Lorentz force modulus $|\mathbf{J} \times \mathbf{B}|(r)$. The results are shown below, compared to the stability curves for several values of m .

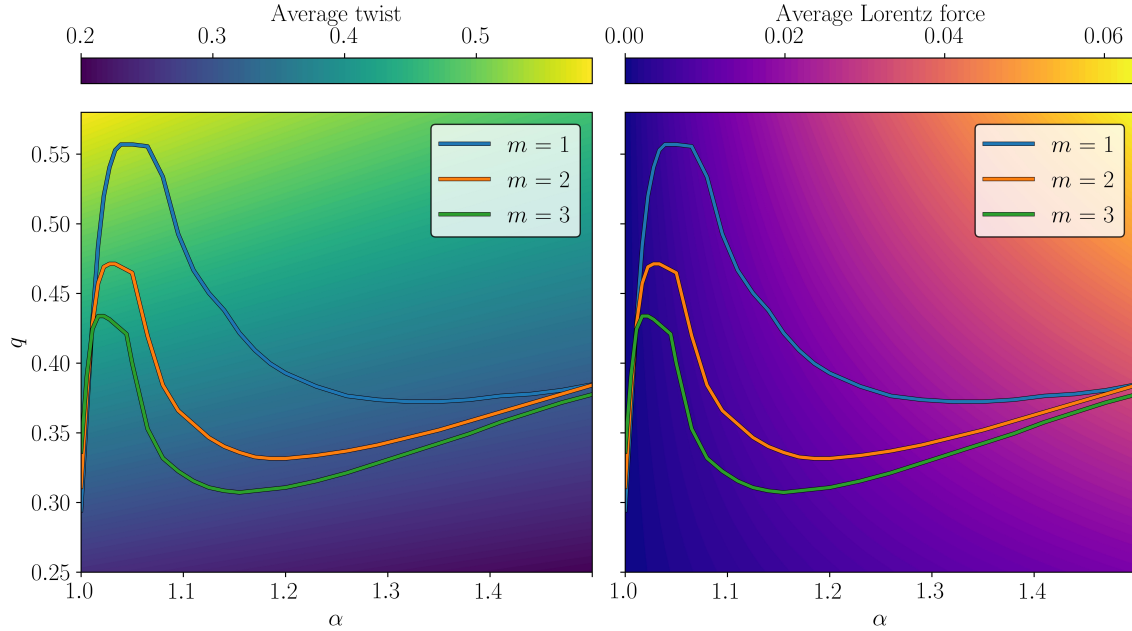


Figure 4.8: Stability curves for different instability types, compared to both average twist and average Lorentz forces within the MFR. The arbitrary growth rate threshold $\lambda = 10^{-7}$ is being employed. The units of the Lorentz force are such that $\mu_0 = 1$.

The first plot shows how, in general, the highly twisted configurations are unstable to perturbations of all azimuthal wave numbers m . Moreover, for larger values of α , there seems to be a good correlation between the stability curve and the level curves of the average twist, which reinforces the backs the statement that the average twist is generally a good indicator of MFR stability. On the other hand, the plot to the right reinforces what we already knew: there are configurations with no forces that are unstable, while other parametric regions leading to much higher forces that are found to be stable.

Finally, the superstability shown in the stability curves for $\alpha \approx 1.05$ is still to be discussed. For what has been seen so far, the twist within the flux rope seems to have the highest relation to the instabilities taking place in MFRs. If we look at the twist distribution for the values of α corresponding to this superstability, see Figure 4.3, we can see the twist is zero at the axis but very rapidly increases towards q . Hence, it could be that sudden changes in the internal twist could cause the MFR to be particularly stable. It is also key to notice the superstability area is particularly force-free, which also suggests that the twist of the MFR could be causing such phenomenon. Nevertheless, other potential drivers of instabilities should also be considered before drawing any definite conclusions on the matter.

5 . Conclusions

In this work, we have worked on the determination of growth rates for the instabilities of a cylindrical MFR with a free boundary, following both fundamental and practical approaches.

On the theoretical side, a quite robust justification of the growth rate method for a plasma with arbitrary geometry has been given. One of the new features of this work has been to consider displacements belonging to the space of test functions, which has proven to be an appropriate setting to study localized smooth perturbations of the equilibrium. However, several assumptions have been made with no proof, such as the uniqueness of solutions for the equation of motion, the existence of a minimal mode and the discreteness of the spectra of the ideal MHD force operator. In the future, it would be interesting to evaluate whether these assumptions hold, or if they can be relaxed by providing a simpler justification of the method.

Moreover, all the equations in the method developed in [Linton et al. \(1996\)](#) have been successfully reproduced, and they have been adapted to contemplate flux ropes with an arbitrary density distribution and instabilities of any azimuthal wave number m . Nevertheless, the validity of considering Fourier harmonic displacements in order to carry out the optimization of the generalized energy has not been rigorously justified, and would be a topic worth thinking about in the future.

Then, the method has been applied to our modification of the Gold-Hoyle model, leading to several conclusions regarding instabilities of all orders m . The sausage instability ($m = 0$) has been found to be stable. On the other hand, instabilities have been found for all $m \geq 1$, and displacements with negative order have been shown to exhibit symmetrical behavior, as expected. The growth rates of such instabilities have been shown to be maximum for axial wave numbers $k \approx -mq$, which can be regarded as a generalization of a well known result for the kink instabilities in the Gold-Hoyle model.

The behavior of the instabilities when increasing the twist parameter q has been an increase in the growth rate of instabilities of every order, which has allowed us to define stability curves for given growth rate thresholds λ_0 , providing us with a simple way to analyze the stability of each equilibrium magnetic field configuration (α, q) . When increasing the force parameter α from the force-free setting $\alpha = 1$, two important conclusions have been reached. Firstly, we have seen that the presence of Lorentz forces within a magnetic flux rope structure, even if they are in opposite directions and oriented inwards near the edge, does not necessarily lead to more unstable configurations, despite the hypothesis suggested in [Florido-Llinas et al. \(2020\)](#).

Secondly, the presence of Lorentz forces has led to an inversion in dominance between the different classes m of instability: in a force-free configuration the kink instabilities were dominant, but when setting $\alpha > 1$ we saw that larger values of m can attain even higher growth rates. This can be thought of as a counter example to the potential generalization of the comparison theorem from [Newcomb \(1960\)](#), adapting it to the modern stability definition introduced in [Goedbloed \(1974\)](#).

A superstability phenomenon has been observed at $\alpha \approx 1.05$ for all kinds of instability, although it became less prominent for larger values of m . An explanation for this has been proposed, based on a hypothetical stabilizing effect of MFR configurations with a large increase in twist near the axis. However, there is not a great basis for that assumption, and should definitely be explored in the future by using other MFR models which lead to a similar twist. It would be very insightful to design another MFR model starting from a force-free configuration, such as the well known

Lindquist model, and evaluate which of our conclusions transfer well to it.

Finally, other longer term goals for this method include trying to predict growth rates in interpretable units, and compare them with CME observations. It would also be key to adapt the equations to more complex geometries, such as curved axis and distorted cross-section, and even non-symmetrical geometries, which allowed to conduct a proper modeling of the solar wind's magnetic field outside the MFR.

Bibliography

- G. K. Ananthasuresh. First variation of a functional [Lecture 11c]. *Structural Optimization; Size, Shape, and Topology*, Aug. 2021. [\[URL\]](#).
- I. B. Bernstein, E. A. Frieman, M. D. Kruskal, and R. M. Kulsrud. An energy principle for hydro-magnetic stability problems. *Proceedings of the Royal Society of London. Series A. Mathematical and Physical Sciences*, 244(1236):17–40, Feb. 1958. DOI. [\[URL\]](#).
- F. Carcaboso, R. Gómez-Herrero, F. Espinosa Lara, M. A. Hidalgo, I. Cernuda, and J. Rodríguez-Pacheco. Characterisation of suprathermal electron pitch-angle distributions: Bidirectional and isotropic periods in solar wind. *Astronomy & Astrophysics*, 635:A79, Mar. 2020. DOI. [\[URL\]](#).
- R. Cristoferi. Calculus of variations: lecture notes. *Mellon College of Science*, May 2016. [\[URL\]](#).
- M. Florido-Llinas. Study of the kink instability and twist distribution of heliospheric magnetic flux ropes (Bachelor’s thesis). *UPC Commons*, May 2020. [\[URL\]](#).
- M. Florido-Llinas, T. Nieves-Chinchilla, and M. G. Linton. Analysis of the Helical Kink Stability of Differently Twisted Magnetic Flux Ropes. *Solar Physics*, 295(9):118, Sept. 2020. DOI. [\[URL\]](#).
- J. P. Freidberg. *Plasma Physics and Fusion Energy*. Cambridge University Press, Cambridge, 2007. DOI. [\[URL\]](#).
- J. P. Goedbloed. New approach to magnetohydrodynamic stability: I. A practical stability concept. *Physics of Fluids*, 17(5):908, 1974. DOI. [\[URL\]](#).
- J. P. Goedbloed. MHD instabilities in astrophysical plasmas: very different from MHD instabilities in tokamaks! *Plasma Physics and Controlled Fusion*, 60(1):014001, Jan. 2018. DOI. [\[URL\]](#).
- J. P. H. Goedbloed and S. Poedts. *Principles of Magnetohydrodynamics*. Cambridge University Press, 1 edition, Aug. 2004. DOI. [\[URL\]](#).
- T. Gold and F. Hoyle. On the Origin of Solar Flares. *Monthly Notices of the Royal Astronomical Society*, 120(2):89–105, Feb. 1960. DOI. [\[URL\]](#).
- A. Gsponer. Physics of high-intensity high-energy particle beam propagation in open air and outer-space plasmas. *arXiv:physics/0409157*, Jan. 2009. [\[URL\]](#). arXiv: physics/0409157.
- F. E. Harris. Series Solutions: Important ODEs. In *Mathematics for Physical Science and Engineering*, pages 487–543. Elsevier, 2014. DOI. [\[URL\]](#).
- A. Hassanin and B. Kliem. Helical kink instability in a confined solar eruption. *The Astrophysical Journal*, 832(2):106, Nov. 2016. DOI. [\[URL\]](#).
- Q. Hu and B. U. Sonnerup. Reconstruction of magnetic flux ropes in the solar wind. *Geophysical Research Letters*, 28(3):467–470, Feb. 2001. DOI. [\[URL\]](#).
- J. K. Hunter. Lecture Notes on Parcial Differential Equations. Chapter 1: Preliminaries. *UC Davis, Department of Mathematics*, June 2014. [\[URL\]](#).

- G. Karniadakis. Numerical Solution of Partial Differential Equations II: Self-adjoint operators and complete orthonormal bases. *Brown University, Center for Fluid Mechanics*, pages 71–77, June 2015. [\[URL\]](#).
- K. J. Knizhnik, M. G. Linton, and C. R. DeVore. The Role of Twist in Kinked Flux Rope Emergence and Delta-spot Formation. *The Astrophysical Journal*, 864(1):89, Sept. 2018. DOI. [\[URL\]](#).
- G. Laval, C. Mercier, and R. Pellat. Necessity of the energy principles for magnetostatic stability. *Nuclear Fusion*, 5(2):156–158, June 1965. DOI. [\[URL\]](#).
- A. E. Lifschitz. Magnetohydrodynamics and spectral theory. *Developments in electromagnetic theory and applications*, 1989. [\[URL\]](#).
- M. G. Linton, D. W. Longcope, and G. H. Fisher. The Helical Kink Instability of Isolated, Twisted Magnetic Flux Tubes. *The Astrophysical Journal*, 469:954, Oct. 1996. DOI. [\[URL\]](#).
- J. J. Masías-Meza, S. Dasso, P. Démoulin, L. Rodriguez, and M. Janvier. Superposed epoch study of ICME sub-structures near Earth and their effects on Galactic cosmic rays. *Astronomy & Astrophysics*, 592:A118, Aug. 2016. DOI. [\[URL\]](#).
- C. Möstl, C. J. Farrugia, H. K. Biernat, M. Leitner, E. K. J. Kilpua, A. B. Galvin, and J. G. Luhmann. Optimized Grad – Shafranov Reconstruction of a Magnetic Cloud Using STEREO-Wind Observations. *Solar Physics*, 256(1-2):427–441, May 2009. DOI. [\[URL\]](#).
- W. A. Newcomb. Hydromagnetic stability of a diffuse linear pinch. *Annals of Physics*, 10(2):232–267, June 1960. DOI. [\[URL\]](#).
- T. Nieves-Chinchilla, M. G. Linton, M. A. Hidalgo, A. Vourlidas, N. P. Savani, A. Szabo, C. Farrugia, and W. Yu. A circular-cylindrical flux-rope analytical model for magnetic clouds. *The Astrophysical Journal*, 823(1):27, May 2016. DOI. [\[URL\]](#).
- T. Nieves-Chinchilla, M. G. Linton, M. A. Hidalgo, and A. Vourlidas. Elliptic-cylindrical Analytical Flux Rope Model for Magnetic Clouds. *The Astrophysical Journal*, 861(2):139, July 2018. DOI. [\[URL\]](#).
- K. Nishikawa and M. Wakatani. Plasma Physics: Basic Theory with Fusion Applications. *Springer*, Aug. 2000. DOI. [\[URL\]](#).
- E. Priest. *Magnetohydrodynamics of the Sun*. Cambridge University Press, Cambridge, 2013. DOI. [\[URL\]](#).
- H. Smith. Spectral theory for compact self-adjoint operators. *University of Washington, Department of Mathematics*, 2015. [\[URL\]](#).
- A. Vourlidas, R. Colaninno, T. Nieves-Chinchilla, and G. Stenborg. The first observation of a rapidly rotating coronal mass ejection in the middle corona. *The Astrophysical Journal*, 733(2):L23, June 2011. DOI. [\[URL\]](#).
- A. J. Weiss, T. Nieves-Chinchilla, C. Möstl, M. A. Reiss, T. Amerstorfer, and R. L. Bailey. Generally Curved Magnetic Flux Rope Structures. *arXiv:2202.10096 [astro-ph, physics:physics]*, Feb. 2022. [\[URL\]](#). arXiv: 2202.10096.
- V. Zakharov. Bessel Functions and their Applications to Solutions of Partial Differential Equations. *Math 456 Lecture Notes*, 2009. [\[URL\]](#).